The Astrophysical Journal, 835:88 (27pp), 2017 January 20 doi:10.3847/1538-4357/835/1/88

THE FMOS-COSMOS SURVEY OF STAR-FORMING GALAXIES AT $z \sim 1.6$. IV. EXCITATION STATE AND CHEMICAL ENRICHMENT OF THE INTERSTELLAR MEDIUM

D. Kashino[1], J. D. Silverman[2], D. Sanders[3], J. S. Kartaltepe[4], E. Daddi[5], A. Renzini[6], F. Valentino[5,7], G. Rodighiero[8], S. Juneau[5], L. J. Kewley[9], H. J. Zahid[10], N. Arimoto[11,12], T. Nagao[13], J. Chu[3], N. Sugiyama[14], F. Civano[15,16], O. Ilbert[17], M. Kajisawa[13,18], O. Le Fèvre[17], C. Maier[19], D. Masters[20], T. Miyaji[21], M. Onodera[11,12], A. Puglisi[8], and Y. Taniguchi[22]

[1] Institute for Astronomy, Department of Physics, ETH Zürich, Wolfgang-Pauli-strasse 27, CH-8093 Zürich, Switzerland; kashinod@phys.ethz.ch
[2] Kavli Institute for the Physics and Mathematics of the Universe (WPI), Todai Institutes for Advanced Study, the University of Tokyo, Kashiwanoha, Kashiwa, 277-8583, Japan
[3] Institute for Astronomy, University of Hawaii, 2680 Woodlawn Drive, Honolulu, HI 96822, USA
[4] School of Physics and Astronomy, Rochester Institute of Technology, 84 Lomb Memorial Dr., Rochester, NY 14623, USA
[5] Laboratoire AIM-Paris-Saclay, CEA/DSM-CNRS-Université Paris Diderot, Irfu/Service d'Astrophysique, CEA-Saclay, Service d'Astrophysique, F-91191 Gif-sur-Yvette, France
[6] INAF Osservatorio Astronomico di Padova, vicolo dell'Osservatorio 5, I-35122 Padova, Italy
[7] Dark Cosmology Centre, Niels Bohr Institute, University of Copenhagen, Juliane Mariesvej 30, DK-2100 Copenhagen, Denmark
[8] Dipartimento di Fisica e Astronomia, Universitá di Padova, vicolo dell'Osservatorio, 2, I-35122 Padova, Italy
[9] Research School of Astronomy and Astrophysics, Australian National University, Cotter Road, Weston Creek, ACT 2611, Australia
[10] Smithsonian Astrophysical Observatory, Harvard-Smithsonian Center for Astrophysics, 60 Garden Street, Cambridge, MA 02138, USA
[11] Subaru Telescope, National Astronomical Observatory of Japan, National Institutes of Natural Sciences (NINS), 650 North Aohoku Place, Hilo, HI 96720, USA
[12] Department of Astronomical Science, SOKENDAI (The Graduate University for Advanced Studies), 2-21-1 Osawa, Mitaka, Tokyo, Japan
[13] Research Center for Space and Cosmic Evolution, Ehime University, Bunkyo-cho 2-5, Matsuyama 790-8577, Japan
[14] Division of Particle and Astrophysical Science, Graduate School of Science, Nagoya University, Nagoya, 464-8602, Japan
[15] Yale Center for Astronomy and Astrophysics, 260 Whitney Avenue, New Haven, CT 06520, USA
[16] Harvard-Smithsonian Center for Astrophysics, 60 Garden Street, Cambridge, MA 02138, USA
[17] Aix-Marseille Université, CNRS, LAM (Laboratoire d'Astrophysique de Marseille), UMR 7326, F-13388 Marseille, France
[18] Graduate School of Science and Engineering, Ehime University, Bunkyo-cho 2-5, Matsuyama, Ehime, 790-8577, Japan
[19] University of Vienna, Department of Astrophysics, Türkenschanzstrasse 17, A-1180 Vienna, Austria
[20] Infrared Processing and Analysis Center, California Institute for Technology, MC 100-22, 770 South Wilson Ave, Pasadena, CA 91125, USA
[21] Instituto de Astronomía sede Ensenada, Universidad Nacional Autónoma de México, Km. 103, Carret. Tijunana-Ensenada, Ensenada, BC, Mexico
[22] The Open University of Japan 2-11 Wakaba, Mihama-ku, Chiba 261- 8586 Japan
Received 2016 April 15; revised 2016 November 25; accepted 2016 December 4; published 2017 January 20

ABSTRACT

We investigate the physical conditions of ionized gas in high-z star-forming galaxies using diagnostic diagrams based on the rest-frame optical emission lines. The sample consists of 701 galaxies with an Hα detection at $1.4 \lesssim z \lesssim 1.7$, from the Fiber Multi-Object Spectrograph (FMOS)-COSMOS survey, that represent the normal star-forming population over the stellar mass range $10^{9.6} \lesssim M_*/M_\odot \lesssim 10^{11.6}$, with those at $M_* > 10^{11}\,M_\odot$ being well sampled. We confirm an offset of the average location of star-forming galaxies in the Baldwin–Phillips–Terlevich (BPT) diagram ([O III]/Hβ versus [N II]/Hα), primarily toward higher [O III]/Hβ, compared with local galaxies. Based on the [S II] ratio, we measure an electron density ($n_e = 220^{+170}_{-130}$ cm^{-3}), which is higher than that of local galaxies. Based on comparisons to theoretical models, we argue that changes in emission-line ratios, including the offset in the BPT diagram, are caused by a higher ionization parameter both at fixed stellar mass and at fixed metallicity, with additional contributions from a higher gas density and possibly a hardening of the ionizing radiation field. Ionization due to active galactic nuclei is ruled out as assessed with *Chandra*. As a consequence, we revisit the mass–metallicity relation using [NII]/Hα and a new calibration including [N II]/[S II] as recently introduced by Dopita et al. Consistent with our previous results, the most massive galaxies ($M_* \gtrsim 10^{11}\,M_\odot$) are fully enriched, while those at lower masses have metallicities lower than local galaxies. Finally, we demonstrate that the stellar masses, metallicities, and star formation rates of the FMOS sample are well fit with a physically motivated model for the chemical evolution of star-forming galaxies.

Key words: galaxies: abundances – galaxies: evolution – galaxies: high-redshift – galaxies: ISM – galaxies: star formation

1. INTRODUCTION

The physical conditions of the interstellar medium (ISM) provide clues to understanding the current state and past activity of star formation and gas reprocessing in galaxies. The study of ionized gas in star-forming (i.e., H II) regions has been carried out through many early observational efforts (e.g., Aller 1942; Pagel et al. 1979, 1980), and the underlying physics has been developed theoretically with photoionization models (e.g., Evans & Dopita 1985; Dopita et al. 2000; Kewley & Dopita 2002). Numerous efforts to study the ISM in low-redshift galaxies ($z \lesssim 0.3$) are based on large spectroscopic data sets such as the Sloan Digital Sky Survey (SDSS; e.g., Kauffmann et al. 2003a; Brinchmann et al. 2004; Tremonti et al. 2004). A wide variety of empirical diagnostics of the gas properties have been established, especially based on spectral features in the rest-frame optical window.

In particular, the Baldwin–Phillips–Terlevich (BPT; Baldwin et al. 1981; Veilleux & Osterbrock 1987) diagnostic diagram compares line ratios [N II]/Hα and [O III]/Hβ to distinguish star-forming galaxies from those hosting and/or dominated by an active galactic nucleus (AGN). Local star-forming galaxies form a tight "abundance sequence" in the BPT diagram (e.g.,

Kauffmann et al. 2003a) with ionization attributed to radiation from young massive stars (types O and B). In contrast, AGNs deviate from this sequence due to harder radiation from an accretion disk. Large data sets such as SDSS have established a precise location of star-forming galaxies and AGNs, thus facilitating a relatively clean selection of these populations.

However, the ISM properties of galaxies at higher redshifts ($z \gtrsim 1$), where most key rest-frame optical emission lines are redshifted into the infrared, are still unclear. One would expect the properties of ionized gas in high-z galaxies to be dissimilar to those in local galaxies given the latter's higher star formation rate (SFR) (see Madau & Dickinson 2014 for a review) and higher gas fraction (e.g., Genzel et al. 2010; Magdis et al. 2012; Scoville et al. 2014). Over the last decade, the universality of the BPT diagram for high-redshift galaxies has been examined through near-infrared spectroscopic campaigns. Early studies have reported an offset of the distribution of star-forming galaxies at higher redshifts ($z \sim 1$–3) from the local abundance sequence based on relatively small samples (e.g., Shapley et al. 2005; Erb et al. 2006; Liu et al. 2008). More recently, the offset has been reaffirmed using larger samples (e.g., Steidel et al. 2014; Zahid et al. 2014b; Hayashi et al. 2015; Kartaltepe et al. 2015; Shapley et al. 2015) observed with multi-object near-infrared spectrographs. However, the amount of the offset in the BPT diagram and other emission-line diagrams has not been firmly established across the general star-forming population at the various epochs since the location of galaxies on such diagrams can be significantly affected by sample selection (see Juneau et al. 2014; Shapley et al. 2015; Cowie et al. 2016). These offsets likely reflect more extreme conditions of H II gas in high-z galaxies such as having a higher value of the ionization parameter ($q_{\rm ion}$), i.e., the ratio of the number density of ionizing photons to the density of hydrogen atoms in H II regions, or a harder radiation field implied by the presence of metal-poor, Fe-depleted stars and/or massive binaries (Steidel et al. 2014, 2016; Kewley et al. 2015; Cowie et al. 2016). Alternative explanations are an enhancement of the nitrogen-to-oxygen abundance ratio and high gas pressure (e.g., Masters et al. 2014; Shirazi et al. 2014; Cowie et al. 2016; Sanders et al. 2016). However, it still remains unsettled what physical factors cause the BPT offset and other changes in the emission-line ratios of high-z galaxies.

Directly related to diagnostics of ionization, the gas-phase metallicity (hereafter metallicity) is an important probe of the evolution of galaxies as a tool to trace past star formation history. The abundance of an element from nucleosynthesis is further influenced by both inflowing gas that dilutes the metal fraction of the ISM, and outflows that transpose metals into the circumgalactic environment (e.g., Köppen & Edmunds 1999; Dalcanton 2007; Ellison et al. 2008; Erb 2008; Finlator & Davé 2008; Cresci et al. 2010; Mannucci et al. 2010; Peeples & Shankar 2011; Bouché et al. 2012; Lilly et al. 2013). In the local universe, a correlation between stellar mass and metallicity has been robustly established based on large data sets such as SDSS (e.g., Tremonti et al. 2004; Zahid et al. 2011; Andrews & Martini 2013). The existence of a mass–metallicity (MZ) relation has been extended up to $z \sim 3$ or more (e.g., Erb et al. 2006; Maiolino et al. 2008; Yabe et al. 2012, 2014, 2015; Maier et al. 2014, 2015; Wuyts et al. 2014; Zahid et al. 2014a, 2014b; Sanders et al. 2015; Onodera et al. 2016) with an evolution where the metallicity decreases with redshift at a fixed stellar mass. We have previously reported an MZ relation at $z \sim 1.6$ (Zahid et al. 2014b), using a smaller subset of the data from the Fiber Multi-Object Spectrograph (FMOS)-COSMOS program (Silverman et al. 2015), that shows the most massive galaxies as being fully mature at a level similar to local massive galaxies while lower-mass galaxies are less enriched than local galaxies. However, there still remain some discrepancies between various studies that implement different sample selection methods and/or metallicity determinations.

An anticorrelation between metallicity and SFR at a fixed stellar mass has been seen in local galaxies (e.g., Ellison et al. 2008). In particular, Mannucci et al. (2010) introduced the SFR as a third parameter in the MZ relation, and proposed the existence of a universal relation between these three quantities, referred to as the fundamental metallicity relation (FMR). Several studies have found that introducing the FMR reduces the scatter relative to the MZ relation (Lara-López et al. 2010b, 2013; Mannucci et al. 2011; Yates et al. 2012; Zahid et al. 2014b), although the actual shape of the FMR may differ appreciably from one study to another due to differences in sample selection and/or in the adopted metallicity indicator (e.g., Andrews & Martini 2013). The apparent SFR–Z anticorrelation is interpreted as resulting from upward fluctuations of the infall rate of pristine/metal-poor gas boosting the SFR while diluting the metallicity of the ISM (Ellison et al. 2008; Mannucci et al. 2010), as supported by several analytic studies and numerical simulations (e.g., Davé et al. 2012; Dayal et al. 2013; Lilly et al. 2013). Measuring the M_*–Z–SFR relation at all redshifts is an essential step toward our understanding of star formation and the chemical evolution of galaxies. However, beyond the local universe, the existence and shape of the FMR has not been firmly established yet (see e.g., Steidel et al. 2014; Wuyts et al. 2014; Yabe et al. 2014; Zahid et al. 2014b; Salim et al. 2015; Sanders et al. 2015; Guo et al. 2016).

To further understand the typical characteristics of high-z H II regions, it is highly desirable to construct a well-controlled sample of typical star-forming galaxies at each epoch. With the availability of multi-object near-infrared spectrographs (i.e., MOSFIRE, FMOS, KMOS) on large telescopes, we can access key rest-frame optical emission lines such as Hβ, [O III] λ5007, Hα, [N II] λ6584, and [S II] $\lambda\lambda$6717, 6731 for samples consisting of up to 10^3 galaxies at $z \gtrsim 1$ (e.g., Rudie et al. 2012; Kriek et al. 2015; Tonegawa et al. 2015). In this paper, we use a sample of Hα-detected galaxies that trace the star-forming main sequence over a stellar mass range $10^{9.6} \lesssim M_*/M_\odot \lesssim 10^{11.6}$, from the FMOS-COSMOS survey (Silverman et al. 2015) to study the typical properties of H II regions of galaxies at $1.43 \leqslant z \leqslant 1.74$. The unique advantages of our sample are the large size—with 701 galaxies having an Hα detection, which is four times larger than that used in our previous study (Zahid et al. 2014b)—and the high sampling rate of the massive galaxy population ($M_* > 10^{11}\,M_\odot$). In addition, our target selection is primarily based on the K-band photometry, which is a good proxy for stellar mass, and thus tends to avoid significant selection biases, as compared to other samples at similar redshifts (e.g., Steidel et al. 2014; Hayashi et al. 2015). We also highlight that our FMOS observations are much deeper (3–5 hr integration times) than in Yabe et al. (2015) and we have J-band spectra for about half of our sample that cover [O III] and Hβ. We use the rest-frame optical key emission lines to evaluate the ionization and excitation of heavy elements, gaseous metallicity, and electron density of ionized gas while minimizing the impact of AGNs.

This paper is organized as follows. In Section 2, we give an overview of our FMOS-COSMOS survey and describe our

samples and spectral analyses. We present our measurements of the emission-line properties in Section 3. Section 4 discusses the characteristics of H II regions in high-z galaxies. We present the metallicity measurements and a reanalysis of the MZ relation in Section 5. In Section 6, we study the relation between mass, metallicity, and SFR. We finally summarize our results and conclusions in Section 7. Throughout this paper, we use a cosmology with $(h, \Omega_M, \Omega_\Lambda) = (0.7, 0.3, 0.7)$ and assume the Salpeter (1955) initial mass function (IMF; 0.1–100 $M_\odot$). All magnitudes given in this paper are in the AB magnitude system.

2. DATA

2.1. The FMOS-COSMOS Survey Overview

The galaxy sample used in this paper is constructed from the data set of the FMOS-COSMOS survey. Here, we provide an overview of the survey, which is extensively described in Kashino et al. (2013) and Silverman et al. (2015). The FMOS-COSMOS survey is a completed near-infrared spectroscopic survey carried out between 2012 March and 2016 April, designed to detect the Hα and [N II] lines from galaxies at $1.43 < z < 1.74$ with the Fiber Multi-Object Spectrograph (FMOS; Kimura et al. 2010) in high-resolution mode ($R \sim 3000$; 1.6–1.8 μm). The emission-line sensitivity of the H-long grating with an integration time of five hours is $\sim 2 \times 10^{-17}$ erg cm^{-2} s^{-1} for a 5σ detection. In addition to Hα and [N II], the [S II] $\lambda\lambda$6717, 6731 doublet lines can be observed within the H-long window for galaxies at $1.43 < z < 1.67$. At the given spectral resolution, all lines are well separated, and thus do not suffer from any blending issues. The accuracy of the spectroscopic redshift determination is $\Delta z/(1+z) = 2.2 \times 10^{-4}$ (Silverman et al. 2015). Galaxies with a positive detection of an Hα emission line in the H-long spectral window are reobserved with the J-long grating (1.11–1.35 μm; $R \sim 2200$) to detect Hβ and [O III] $\lambda\lambda$4959, 5007, which are essential for determining the excitation states of the ionized gas in star-forming regions. All data are reduced using the FMOS pipeline FIBRE-pac (FMOS Image-Based Reduction Package; Iwamuro et al. 2012).

2.2. Target Selection

In this paper, we utilize a larger catalog of galaxies with spectroscopic redshifts from the FMOS-COSMOS survey than presented in Kashino et al. (2013) and Zahid et al. (2014b). This larger sample is the result of additional FMOS observations carried out between 2013 December and 2014 February that are not reported in Silverman et al. (2015). The characteristics of this sample are statistically equivalent to those used in the aforementioned papers. Here, we give a brief overview of the construction of our galaxy catalog.

Our galaxy sample is based on the COSMOS photometric catalog (McCracken et al. 2012; Ilbert et al. 2013) that includes the Ultra-VISTA/VIRCAM photometry. A magnitude limit of $K_S < 23.5$ is imposed for our sample selection, which provides a high level of completeness ($\sim$85%) in stellar mass of galaxies with $M_* \geqslant 10^{10}\,M_\odot$ (Ilbert et al. 2013). The majority of our sample is selected to have a stellar mass above $10^{9.8}\,M_\odot$ and a photometric redshift $1.46 \leqslant z_{\rm phot} \leqslant 1.72$. These values are derived for each object by fitting the spectral energy distribution (SED) using Le Phare (Arnouts & Ilbert 2011) with population synthesis models (Bruzual & Charlot 2003) and a Chabrier (2003) IMF. Hereafter, we convert all stellar masses to a Salpeter IMF by applying a multiplicative factor of 1.7 (Ilbert et al. 2010).

To achieve a high success rate of detecting the Hα emission line, we calculate the expected Hα flux for each galaxy in the photometric catalog and use these values in our target selection. The prediction of Hα flux represents a total flux from each galaxy (without considering flux loss due to the fiber aperture) calculated with Equation (2) of Kennicutt (1998) from the SFR, which is derived from the SED fitting assuming a constant star formation history (see Silverman et al. 2015 for details). Dust extinction toward the Hα emission line is derived via

$$A(\mathrm{H}\alpha) = 3.325 E_{\rm star}(B-V)/f, \quad (1)$$

where the color excess $E_{\rm star}(B-V)$ is estimated from the SED and a Calzetti et al. (2000) extinction curve is assumed. We note that large uncertainties remain in the conversion between the amount of extinction toward stellar emission and that toward nebular emission, which is likely to depend on the geometrical properties of stars, dust, and star-forming regions. While $f = 0.44$ is canonically applied locally (Calzetti et al. 2000), some studies report higher values between 0.44 and 1 for high-z galaxies based on measurements of the Balmer decrement (e.g., Hα/Hβ) or comparisons between SED-based (or UV-based) SFRs and Hα-SFRs (e.g., Kashino et al. 2013; Price et al. 2014; Koyama et al. 2015; Valentino et al. 2015; Puglisi et al. 2016). Here, we use $f = 0.66$ to calculate predicted Hα fluxes for target galaxies. In early pilot observations, a predicted Hα flux threshold of 4×10^{-17} erg cm^{-2} s^{-1} is set without taking into account the aperture loss of $\sim$50%. In the subsequent intensive program, the limit of the predicted Hα flux was raised to 1×10^{-16} erg cm^{-2} s^{-1}. This flux limit is equivalent to SFR $\sim 20\,M_\odot$ yr^{-1} for galaxies at $z \sim 1.6$ with typical values of dust attenuation. The majority (89%) of our sample have a predicted Hα flux higher than 1×10^{-16} erg cm^{-2} s^{-1}.

2.3. Spectral Fitting

We perform a fitting procedure that utilizes the MPFIT package for IDL (Markwardt 2009) to measure the flux of emission lines and associated error, on both individual and composite spectra. The fitting of key emission lines (Hα, [N II] $\lambda\lambda$6548, 6584, Hβ, [O III] $\lambda\lambda$4959, 5007) present in individual spectra is described in detail elsewhere (Kashino et al. 2013; Silverman et al. 2015). In this study, we further perform a fit to the [S II] $\lambda\lambda$6717, 6731 lines based on redshift determined from Hα.

In our emission-line fitting procedure, the value of each pixel is weighted by the noise spectra, and the pixels that are impacted by the OH airglow mask are excluded from the fit. For composite spectra, we use weights based on the variance estimated by jackknife resampling (see Section 2.8). The continuum is first fit with a linear function to pixels near the emission lines and subtracted from the data. Each emission line is then modeled with a Gaussian profile. The [N II] and Hα lines are simultaneously fit with a single line width. We further fix the ratio [N II] λ6584/[N II] λ6548 to the laboratory value of 2.86, and the line width of [S II] to that of Hα. The Hβ and [O III] lines are modeled independently from Hα+[N II] with the ratio of the [O III] doublet fixed to 2.98. This avoids any systematic effects due to uncertainties of the wavelength calibration and provides an independent evaluation of key lines

Table 1
Summary of Emission-line Detections of the FMOS Sample[a]

Emission Lines	*H*-long		*H* and *J*-long	
	Sample-1[b]	w/o AGNs[c]	Sample-2[d]	w/o AGNs
Hα	701 (500)	642 (469)	310 (241)	283 (224)
[N II]	436 (278)	383 (233)	216 (133)	190 (110)
[S II]	77 (17)	73 (17)	32 (5)	31 (5)
Hβ	⋯	⋯	138 (99)	127 (94)
[O III]	⋯	⋯	171 (160)	158 (147)
Hα + [N II] [e]	436 (246)	383 (217)	216 (115)	190 (99)
Hα + [S II]	77 (17)	73 (17)	32 (5)	31 (5)
Hα + [N II] + [S II]	61 (13)	57 (13)	28 (2)	27 (2)
[O III] + Hβ	⋯	⋯	121 (70)	110 (67)
Hα + [N II] + [O III] + Hβ	⋯	⋯	87 (40)	76 (37)
Hα + [S II] + [O III] + Hβ	⋯	⋯	19 (5)	18 (5)
$N_{\rm stack}$[f]	⋯	554	⋯	246

Notes.
[a] The threshold S/N is 3 for Hα and 1.5 for other lines. In parentheses, the numbers of detections with a higher S/N (>5 for Hα and >3 for other lines) are listed.
[b] Sample-1 consists of 701 galaxies with a positive Hα detection.
[c] The numbers of galaxies after the exclusion of AGNs (see Section 2.6.)
[d] Sample-2 consists of 310 galaxies with both a positive Hα detection and an additional *J*-long spectrum.
[e] The numbers of galaxies with multiple emission-line detections are listed in the 6th–11th rows (see Section 2.5).
[f] The numbers of objects that are used for stacking ($1.43 \leqslant z \leqslant 1.67$; AGNs are excluded; see Section 2.8).

(e.g., Hα, [O III]). The observed line widths of Hα and the [O III]–Hβ system agree with each other on average.

2.4. Correction for Balmer Absorption

Stellar atmospheric absorption lowers the observed flux of the Balmer emission lines, in particular Hβ (e.g., Nakamura et al. 2004; Groves et al. 2012). Therefore, we correct the observed Hβ flux for this underlying absorption as a function of stellar mass as given in Zahid et al. (2014b):

$$f_{\rm corr} = \max\,[1,\ 1.02 + 0.30\log\,(M_*/10^{10}\,M_\odot)]. \qquad (2)$$

This relation has been converted to be used with a Salpeter IMF. We apply the absorption correction to the observed Hβ flux of individual galaxies in our FMOS sample, and the measurements based on the composite spectra. The Hα flux is not corrected for the stellar absorption since the flux loss is expected to be negligible (<a few per cent; see Kashino et al. 2013).

The Balmer absorption correction reduces the [O III]/Hβ ratio by 11% on average and maximally by 50% at the high-mass end. The typical amount of this correction is consistent with Shapley et al. (2015) and Steidel et al. (2014). The application of such a correction does not affect our scientific conclusions. We note that the Balmer absorption correction is applied for only the FMOS sample, and not for the local galaxies from the MPA/JHU catalog (see Section 2.9), in which the correction is already taken into account by measuring the emission-line intensities after subtraction of the stellar continuum based on a population synthesis model (see Tremonti et al. 2004 for details).

2.5. Sample Selection for Analysis

In this study, we use 701 galaxies (approximately 40% of observed galaxies) having a detection of the Hα emission line with a signal-to-noise ratio (S/N) greater than 3 in the *H*-long spectrum. The range of spectroscopic redshift is $1.43 \leqslant z \leqslant 1.74$. We define two subsamples based on the spectral coverage. *Sample-1* consists of all 701 galaxies with a positive Hα detection in the *H*-long band, regardless of the presence or absence of the *J*-long coverage. *Sample-2* consists of 310 galaxies (a subset of Sample-1) having additional *J*-long coverage. The numbers of detections of each emission line are summarized in Table 1. For the [S II] doublet, we count the number of objects with both [S II] lines detected at either S/N > 1.5 or >3. The numbers of galaxies with simultaneous detections of multiple emission lines are provided as well. We further group galaxies by the S/N of their emission-line measurements: high quality (HQ) if S/N > 5 for Hα and S/N > 3 for other lines and low quality (LQ) if S/N > 3 for Hα and S/N > 1.5 for others. For stacking analyses (see Section 2.8), galaxies are restricted to those having a redshift measurement in the range $1.43 \leqslant z \leqslant 1.67$ to cover all the key emission lines including [S II] $\lambda\lambda$6717, 6731. The numbers of galaxies used for the stacking analysis are given in the bottom row in Table 1.

2.6. Identification of AGNs

AGNs are excluded for a clean investigation of the conditions of H II regions of star-forming galaxies. In our sample, we identify 22 objects (3%) associated with an X-ray point source in the catalog provided by the *Chandra*-COSMOS Legacy survey (Elvis et al. 2009; Civano et al. 2016), which covers the entire FMOS survey area. These X-ray-detected galaxies are likely to host an AGN because such luminous X-ray emission ($L_{\rm X\text{-}ray} \gtrsim 10^{42}$ erg s^{-1} at 0.5–7 keV) is expected to arise from a hot accretion disk. The fraction of the objects with an X-ray detection (3%) is roughly similar to that reported by Silverman et al. (2009, 2% at $z \sim 1$), who utilized a galaxy sample from the 10k catalog of the zCOSMOS-bright survey (Lilly et al. 2007). The X-ray source fraction of our sample reaches 10% at $M_* > 10^{11}\,M_*$. Such an X-ray AGN fraction at the high-mass end is lower than reported at a similar redshift range (∼25%–30%; e.g., Reddy et al. 2005; Bundy et al. 2008; Brusa et al. 2009; Yamada et al. 2009; Mancini et al. 2015). This is

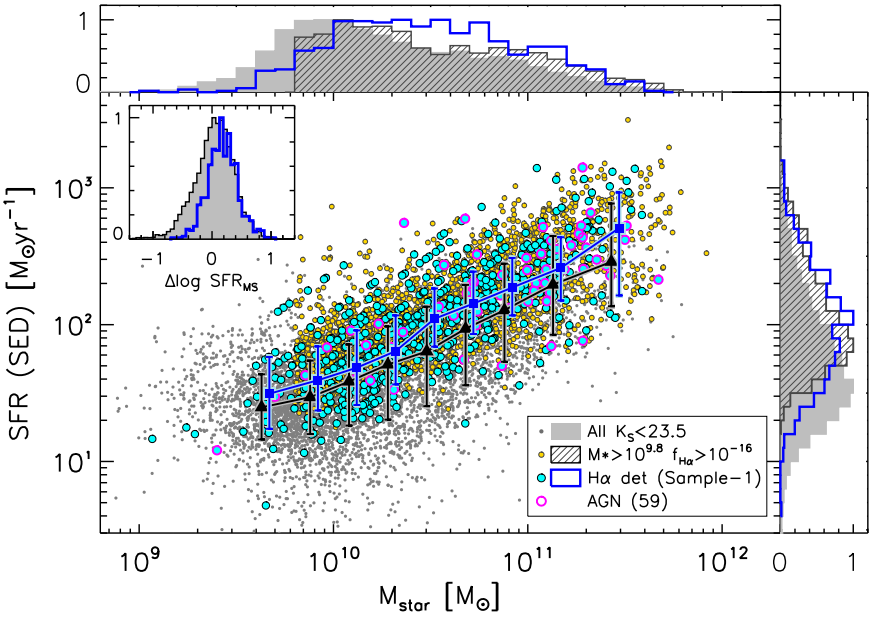

Figure 1. SFR (SED) vs. M_* for galaxies at $1.43 \leqslant z \leqslant 1.74$: all galaxies with $K_S < 23.5$ and $1.46 \leqslant z_{\rm photo} \leqslant 1.72$ in the FMOS survey area (gray dots, filled histograms normalized by their peak values), galaxies with $M_* \geqslant 10^{9.8}\,M_\odot$ and a predicted Hα flux $f(\mathrm{H}\alpha) \geqslant 1 \times 10^{-16}$ erg s^{-1} cm^{-2} (yellow circles, hatched histograms), and galaxies with an Hα detection (cyan circles, blue thick-line histograms) are shown. AGN candidates are marked as magenta circles. The median SFRs in eight stellar mass bins for both the K_S-selected and Hα-detected samples are indicated by large symbols (triangles and squares respectively) with error bars indicating the 68th percentiles. The Hα-detected galaxies trace well the star-forming main sequence, although there is a slight bias toward higher SFRs as compared with the underlying K_S-selected sample (see inset panel).

likely due to the prior selection on the predicted Hα flux applied for galaxies in our sample.

We also flag FMOS sources as AGNs based on their emission-line ratios. While the BPT diagram is commonly used to separate the pure star-forming population and AGNs for low-redshift galaxies, the same boundary is unlikely to be applicable for high-z galaxies (e.g., Kewley et al. 2013b). Here, we use a boundary between star-forming galaxies and AGNs in the BPT diagram at $z = 1.6$ derived by Kewley et al. (2013b) (see Section 3.1). On the basis of their rest-frame optical emission-line properties we identify 39 objects (5.5%) as AGNs that are located above this boundary or have a line ratio of either $\log[\mathrm{N\,II}]/\mathrm{H}\alpha > -0.1$ or $\log[\mathrm{O\,III}]/\mathrm{H}\beta > 0.9$. Of these, four galaxies are detected in the X-ray. The majority of AGNs, identified by their narrow line ratios, are likely obscured (type-II) AGNs. In addition, four objects (less than 1%) have an emission-line width (full width at half maximum) greater than 1000 km s^{-1}, usually Hα, and are taken to be unobscured (type-I) AGNs; one of these is included in the X-ray point source catalog and another object is flagged as AGN based on the line ratios.

In total, 59 objects (8%) are identified as AGNs. The total AGN fraction is roughly consistent with that of Yabe et al. (2014, 6%), who use a sample of star-forming galaxies at $z \sim 1.4$, although they do not have X-ray observations and thus probably miss some AGNs. The AGN fraction increases with stellar mass and reaches 25% at $M_* > 10^{11}\,M_*$. Such a trend is consistent with previous studies (e.g., Xue et al. 2010). Table 1 lists the numbers of galaxies in each sample before and after the exclusion of those hosting AGNs. For stacking analysis, we only use galaxies without an AGN. In the Appendix, we address the additional contribution of AGN photoionization to the stacked emission-line measurements.

2.7. Stellar Masses, SFRs, and the Main Sequence

Stellar masses and SFRs are derived from SED fitting, based on the spectroscopic redshift measured with FMOS, using Le Phare (Arnouts & Ilbert 2011) while assuming a constant star formation history and a Chabrier IMF. Masses and SFRs are converted to a Salpeter IMF by multiplying them by a factor of 1.7. The statistical errors of the derived stellar masses and SFRs are typically 0.05 dex and 0.2 dex, respectively. The sample spans a range of stellar mass $9.6 \lesssim \log M_*/M_\odot \lesssim 11.6$ with a median mass of $\log M_*^{\rm med}/M_\odot = 10.4$. We highlight that our sample includes a large number of very massive galaxies ($M_* \geqslant 10^{11}\,M_\odot$; 120 in total, 92 after removing AGNs; see Section 2.6).

Figure 1 shows the SFR as a function of M_* for our sample, compared with the distribution of K_S-selected ($K_S < 23.5$) galaxies in the equivalent redshift range ($1.46 \leqslant z_{\rm photo} \leqslant 1.72$; 7987; gray dots). The K_S-selected sample shows a clear correlation between stellar mass and SFR (i.e., star-forming main sequence) with a standard deviation around the relation of 0.37 dex. Of these, galaxies with $M_* \geqslant 10^{9.8}\,M_\odot$ and predicted Hα flux $f(\mathrm{H}\alpha) \geqslant 1 \times 10^{-16}$ erg s^{-1} cm^{-2} (2324) are marked as small yellow circles; those with an Hα detection (Sample-1) are shown as cyan circles. Objects identified as AGNs are marked as magenta circles. The Sample-1 galaxies apparently follow the distribution of the parent K_S-selected sample. To quantify a potential bias in our sample, we fit a power-law relation (SFR $\propto M_*^\alpha$) to the K_S-selected and Hα-detected samples separately for galaxies with $M_* \geqslant 10^{9.8}\,M_\odot$. While the slope is consistent between the two samples ($\alpha = 0.66 \pm 0.01$ for the former and 0.68 ± 0.02 for the latter), the Hα-detected sample is slightly biased toward higher SFRs by $\sim$0.15 dex over the entire stellar mass range due to the self-imposed limit on the predicted Hα flux. However, such a

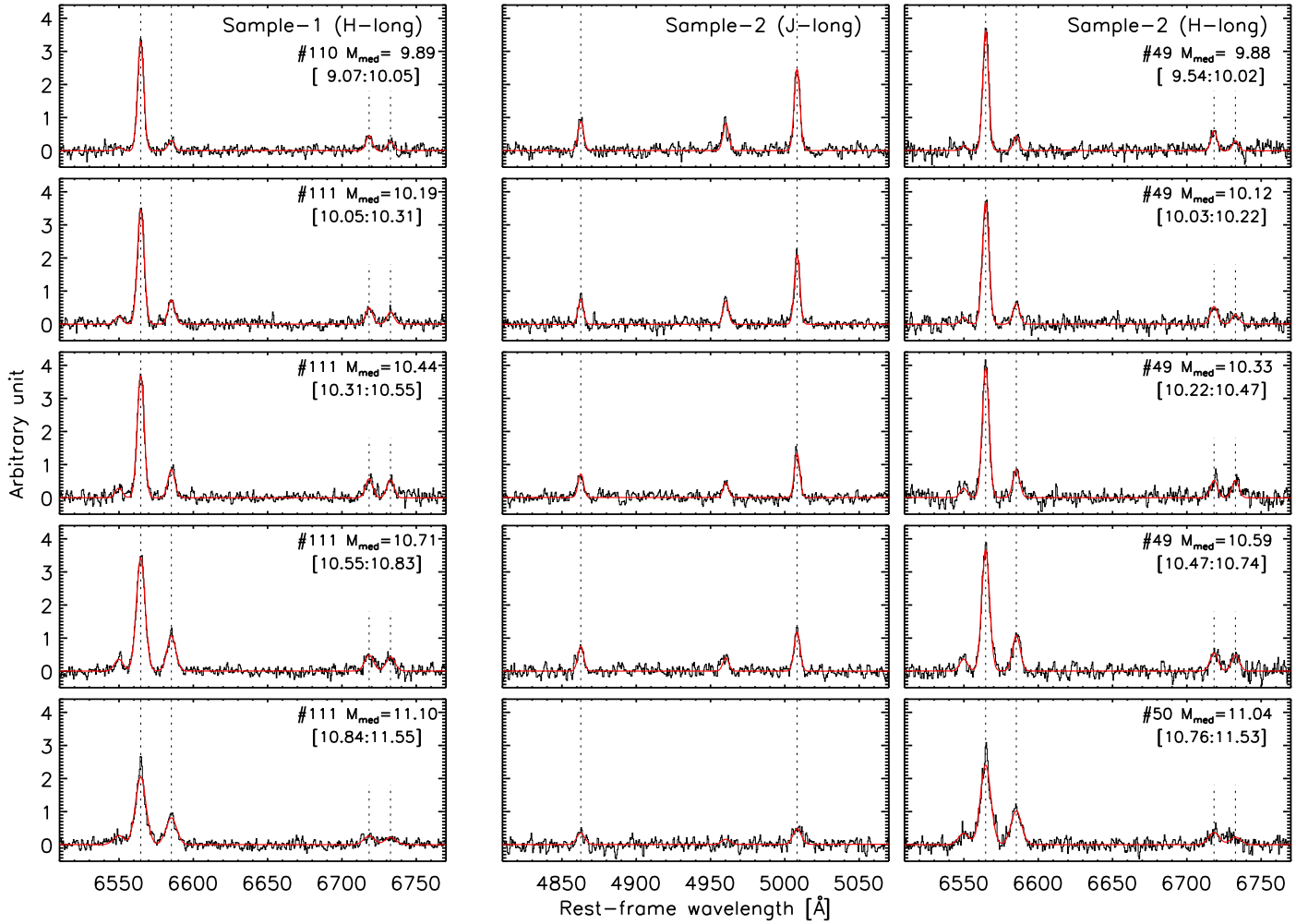

Figure 2. Composite spectra in five bins of stellar mass of Sample-1 (left column) and Sample-2 (middle and right columns). The number of individual spectra is indicated for each bin (e.g., #110). The stellar mass increases from top to bottom, as indicated by their median value ($\log M_*/M_\odot$) and the interval shown in each panel. The observed spectra and the best-fit models are shown by black thin solid lines and red thick curves. Vertical dotted lines show the positions of Hα, [N II] λ6584, [S II] $\lambda\lambda$6717, 6731, Hβ, and [O III] λ5007.

bias is less than half of the scatter of the main sequence. The inset panel shows the normalized distribution of the difference in SFR from the fit to the main sequence for both K_S-selected galaxies (filled gray histogram) and Hα-detected galaxies (blue solid histogram). As is clearly evident, our final sample traces well the star-forming main sequence at $z \sim 1.6$.

We also measure SFRs from the Hα flux measured by FMOS following Equation (2) of Kennicutt (1998). As described in Kashino et al. (2013), the observed Hα fluxes are corrected for the flux falling outside the FMOS 1.″2 diameter fiber. This aperture correction factor is evaluated for each object from a comparison between the observed continuum flux from FMOS spectra and the Ultra-VISTA *H*- and *J*-band photometry (McCracken et al. 2012). The observed Hα flux is also corrected for dust extinction. The amount of extinction (i.e., color excess $E_{\rm star}(B-V)$) is estimated from the SED of each galaxy, then it is converted to the extinction toward the Hα emission line by using Equation (1) with $f = 0.59$. This f value is adjusted to bring observed Hα-based SFRs into agreement with the SED-based SFRs. While we assumed $f = 0.66$ in our target selection (Section 2.2), the application of a different f-factor does not change any of our conclusions.

2.8. Spectral Stacking

We make use of co-added spectra to account for galaxies with faint emission lines and avoid a bias induced by galaxies with the strongest lines (i.e., highest SFR and/or less extinction). Individual spectra of galaxies at $1.43 \leqslant z \leqslant 1.67$ are stacked in bins of stellar mass. This redshift range ensures that all the emission lines used in this study fall within the spectral coverage of FMOS. A fair fraction (30%) of the pixels in individual spectra that are strongly impacted by the OH mask and residual sky lines are removed by identifying them in the noise spectra as regions with relatively large errors as compared with the typical noise level of $\sim 5 \times 10^{-19}$ erg cm^{-2} s^{-1} A^{-1} (see Figure 11 in Silverman et al. 2015). We transform all individual spectra to the rest-frame wavelength based on their redshift and resample them to a common wavelength grid with a spacing of 0.5 Å/pixel. This wavelength sampling is equivalent to the observed-frame spectral resolution of FMOS (1.25 Å/pixel) for galaxies at $z = 1.5$.

After subtracting the continuum, the individual de-redshifted spectra are averaged by using the *resistant_mean.pro*, an IDL routine available in the Astronomy User's Library. We apply a 5σ clipping, which removes data that deviate from the median

Table 2
Emission Line Ratios from Co-added Spectra

Median M_*[a]	M_* Range	$N2$[b]	$S2$[c]	$N2S2$[d]	$O3$[e]
Sample-1					
9.84	9.07–9.94	-1.09 ± 0.12	-0.61 ± 0.07	-0.48 ± 0.13	⋯
10.04	9.95–10.11	-0.87 ± 0.07	-0.61 ± 0.07	-0.25 ± 0.09	⋯
10.21	10.12–10.28	-0.64 ± 0.04	-0.60 ± 0.06	-0.04 ± 0.07	⋯
10.35	10.29–10.44	-0.70 ± 0.05	-0.55 ± 0.05	-0.15 ± 0.07	⋯
10.51	10.44–10.59	-0.55 ± 0.04	-0.52 ± 0.06	-0.03 ± 0.06	⋯
10.69	10.60–10.78	-0.52 ± 0.04	-0.62 ± 0.07	0.10 ± 0.08	⋯
10.85	10.78–11.05	-0.46 ± 0.04	-0.57 ± 0.06	0.12 ± 0.07	⋯
11.16	11.06–11.55	-0.37 ± 0.05	-0.61 ± 0.09	0.24 ± 0.10	⋯
Sample-2					
9.88	9.54–10.02	-0.93 ± 0.08	-0.60 ± 0.09	-0.34 ± 0.11	0.46 ± 0.06
10.12	10.03–10.22	-0.77 ± 0.06	-0.64 ± 0.06	-0.13 ± 0.07	0.43 ± 0.06
10.33	10.22–10.47	-0.67 ± 0.04	-0.56 ± 0.07	-0.11 ± 0.07	0.23 ± 0.07
10.59	10.47–10.74	-0.53 ± 0.04	-0.54 ± 0.05	0.01 ± 0.05	0.14 ± 0.08
11.04	10.76–11.53	-0.37 ± 0.04	-0.60 ± 0.07	0.22 ± 0.08	0.03 ± 0.16

Notes.
[a] Median $\log M_*/M_\odot$ of each mass bin.
[b] $N2 = \log([\mathrm{N\,II}]\lambda 6584/\mathrm{H}\alpha)$.
[c] $S2 = \log([\mathrm{S\,II}]\lambda\lambda 6717, 6731/\mathrm{H}\alpha)$.
[d] $N2S2 = \log([\mathrm{N\,II}]\lambda 6584/[\mathrm{S\,II}]\lambda\lambda 6717, 6731)$.
[e] $O3 = \log([\mathrm{O\,III}]\lambda 5007/\mathrm{H}\beta)$, corrected for Balmer absorption (see Section 2.4).

by more than five times the median absolute deviation at each pixel. We do not apply any weighting scheme so as to avoid possible biases. The associated noise spectra are computed using a jackknife resampling method. The variance at each pixel is given by the following equation:

$$\sigma^2_{\mathrm{jack}} = \frac{N-1}{N}\sum_{i=1}^{N}\left(F_i - \frac{1}{N}\sum_{i=1}^{N}F_i\right)^2 \quad (3)$$

where N is the sample size used for stacking (after a 5σ clip) and F_i is stacked spectra composed of $N-1$ spectra by removing the ith spectrum. Figure 2 shows the composite spectra of Sample-1 and Sample-2 in five bins of stellar mass. We ensure that the reduced χ^2 of the fit to each composite spectrum is approximately unity (0.8–1.2). The errors on the flux measurements and flux ratios for the stacked spectra are calculated from Equation (3) with F_i replaced by an arbitrary quantity (i.e., flux or line ratio) measured on the ith-removed stacked spectrum.

We note that individual spectra are averaged without any renormalization; this may result in a flux-weighted co-added spectrum that is not representative of galaxies with the faintest emission lines. To examine such effects, we normalize each spectrum by the observed amplitude of the Hα line before co-adding. We then find that the results presented in this study do not depend on whether such a scaling is applied or not. All results presented hereafter are based on a stacking analysis without any such renormalization of the individual spectra. Throughout, we measure average emission-line ratios using co-added spectra of Sample-1 and Sample-2 split into eight and five bins of stellar mass, respectively. In Table 2, we list the emission-line ratios and their associated jackknife errors.

To further check the potential impact of residual OH emission and the suppression mask in the stacking, we construct a sample that consists of only galaxies for which the redshifted wavelength of [N II] λ6584 is more than 9 Å from every OH line[23] (∼50% of the full sample) to ensure that the [N II] line is free from OH contamination (see also Stott et al. 2013). We have checked that the results do not change when restricting the analysis to this smaller sample.

2.9. Local Comparison Sample

We extract a sample of local galaxies from the SDSS Data Release 7 (Abazajian et al. 2009) to compare with the ISM properties of our high-z galaxies. The emission-line flux measurements are from the MPA/JHU catalog (Kauffmann et al. 2003b; Brinchmann et al. 2004; Tremonti et al. 2004) based on Data Release 12 (Alam et al. 2015), for which the stellar absorption is taken into account by subtracting a stellar component as determined from a population synthesis model. We use *total* SFRs from the MPA/JHU catalog, for which SFRs within and outside the SDSS fiber aperture are combined. The *in-fiber* SFRs are based on the extinction-corrected Hα luminosities falling within the fiber (Brinchmann et al. 2004), and SFRs outside the fiber are estimated from the SDSS photometry (see Salim et al. 2007). We convert SFRs to a Salpeter IMF from a Kroupa (2001) IMF by multiplying by a factor of 1.5 (Brinchmann et al. 2004).

Stellar masses are derived from *ugriz* photometry with Le Phare (see Zahid et al. 2011 for details) instead of using the JHU/MPA values. Stellar masses from Le Phare are based on a Chabrier IMF and are smaller than those provided by MPA/JHU by approximately 0.2 dex on average, with a dispersion between the two estimates of 0.14 dex. For this study, the stellar masses are converted to a Salpeter IMF.

The SDSS galaxies are selected over a redshift range $0.04 < z < 0.1$ to reduce the effects of redshift evolution. Kewley et al. (2005) report that line measurements are highly biased toward the central area, which may be more quenched when a covering fraction is less than 20%. To avoid such

[23] The list of the OH lines in the FMOS coverage is available at http://www.subarutelescope.org/Observing/Instruments/FMOS/index.html.

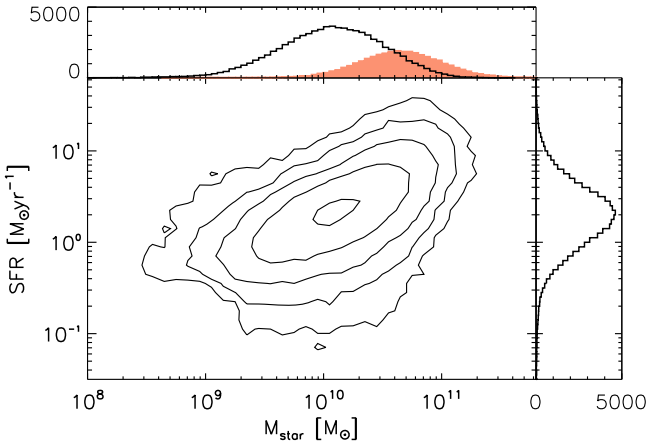

Figure 3. M_* vs. total SFR for local star-forming galaxies from SDSS. Their distributions of stellar mass and SFR are shown by empty histograms. The filled histogram indicates the stellar mass distribution of local AGNs.

aperture effects, we impose a lower redshift limit of 0.04. Furthermore, we require 5σ detections for Hα and 3σ for all other emission lines used in this paper ([N II] λ6584, [S II] $\lambda\lambda$6717, 6731, Hβ, and [O III] λ5007). We classify galaxies as either star-forming or AGNs according to whether they lie below or above the classification line of Kauffmann et al. (2003a) in the BPT diagram (see Section 3.1).

The final sample of local sources consists of 80,003 star-forming galaxies and 31,899 AGNs. In Figure 3, we show the distribution of M_* and total SFR for the SDSS star-forming galaxies. For AGNs, the stellar mass distribution is shown by the filled histogram. The central 99 percentiles of the star-forming galaxies and AGNs include objects with $8.7 < \log M_*/M_\odot < 11.1$ and $9.7 < \log M_*/M_\odot < 11.6$, respectively. We note that our results and conclusions do not change when a different selection is implemented, in which a higher limit is applied for only Hα (S/N > 20) without any S/N limit on the other lines so as to avoid possible biases concerning the detection of faint lines (i.e., Hβ, [N II], and [S II]).

To illustrate the average relations between line ratios and stellar mass of local star-forming galaxies in various diagrams, we split the local star-forming galaxies into the same eight/five stellar mass bins as the FMOS sample or into 24 smaller, equally spaced bins of stellar mass for $10^{8.9} \leqslant M_*/M_\odot \leqslant 10^{11.3}$ (bin size $\Delta \log M_* = 0.1$ dex). For fair comparisons with the FMOS stacked measurements, we define the average line ratios of the SDSS sample as follows. In each bin, we derive the mean luminosities of individual emission lines and calculate the line ratios from these values. To exclude extreme objects, we apply a 3σ clipping in log scales of the luminosities of both Hα and [O III] lines in each bin, which removes approximately 2% of the sample. For the remainder of the paper, we refer to these average line ratios as the *stack* or *stacked line ratios* of the SDSS sample.

The FMOS stacked measurements include objects with no detection of some emission lines, while the SDSS sample consists of those having measurements of all line ratios of interest. Hence it is potentially not straightforward to compare the stacked line ratios of our high-z sample to the *median* or the distribution (e.g., ridge lines of the contours) of all the individual measurements in the reference sample. In fact, the SDSS stacked line ratios are slightly offset from the median values of the individual line ratios or the ridge lines of the contours in various diagrams shown in this paper. These offsets

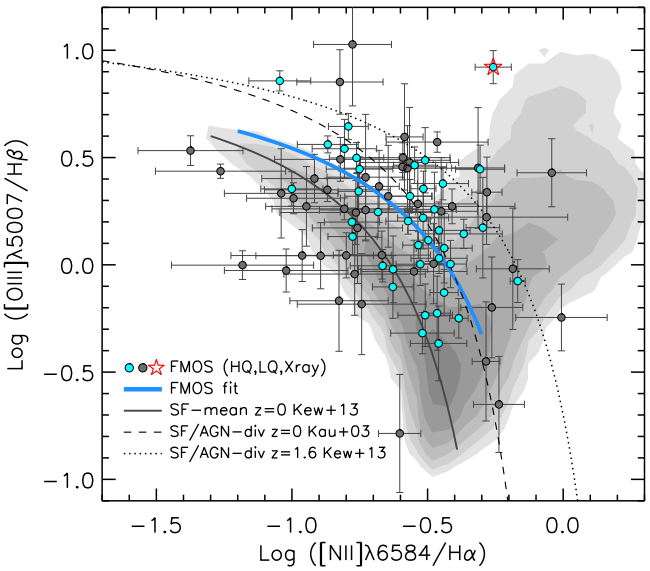

Figure 4. BPT diagnostic diagram: $\log([\mathrm{O\,III}]/\mathrm{H}\beta)$ vs. $\log([\mathrm{N\,II}]/\mathrm{H}\alpha)$. Individual FMOS galaxies (87) are shown with circles for two groups: high quality (HQ, cyan) and low quality (LQ, dark gray). A single object detected in the X-ray band is indicated by a star. Thin curves indicate the empirical abundance sequence of local galaxies given by Equation (4) (solid line: Kewley et al. 2013a), the empirical separation between star-forming galaxies and AGNs for the local SDSS sample (dashed line: Kauffmann et al. 2003a), and the empirical prediction of the division at $z = 1.6$ (dotted line: Kewley et al. 2013b). Shaded contours show the distribution of the local sample (star-forming galaxies plus AGNs) on a log scale. Individual data points from FMOS show an offset from the local sequence, as illustrated by the best fit (thick blue solid line; Equation (5)).

arise from the use of the mean luminosities, which are biased toward more luminous objects, and thus those with higher SFR, while similar effects are potentially expected for the stacked measurements of our FMOS sample. Therefore, this caveat should be kept in mind as long as one relies on the stacking analysis including undetected objects.

3. EMISSION LINE PROPERTIES

3.1. BPT Diagnostic Diagram

We present in Figure 4 the BPT diagram for high-redshift galaxies from our FMOS sample (Sample-2). The line ratios for 87 individual galaxies that have detections of all four lines are indicated by the data points. We illustrate the quality of the measurements by splitting the sample into two groups: high-quality measurements (HQ, S/N > 5 for Hα and S/N > 3 for other relevant lines, i.e., [N II] λ6584, Hβ, and [O III] λ5007) and low-quality ones (LQ, S/N > 3 for Hα and S/N > 1.5 for others). An absorption correction is applied to the observed Hβ fluxes (see Section 2.4). To aid in our interpretation of the high-redshift data, we plot the distribution of line ratios of local SDSS galaxies (star-forming population plus AGNs; see Section 2.6; gray contours). We highlight the local abundance sequence of star-forming galaxies by a commonly used functional form (Kewley et al. 2013a):

$$\log([\mathrm{O\,III}]/\mathrm{H}\beta) = \frac{0.61}{\log([\mathrm{N\,II}]/\mathrm{H}\alpha) + 0.08} + 1.10. \quad (4)$$

More than half of our FMOS galaxies deviate from the above local abundance sequence toward higher [O III]/Hβ and/or higher [N II]/Hα ratios, and a large number of objects are beyond a local demarcation between star-forming galaxies and

AGNs (Kauffmann et al. 2003a). Here it is important to highlight that our sample maps the distribution in the BPT diagram below $\log([\mathrm{O\,III}]/\mathrm{H}\beta) = 0$ down to ~ -0.5 because our sample includes a fairly large number of very massive galaxies (see Figure 1). Kewley et al. (2013b) derive a redshift evolution of the boundary to distinguish star-forming galaxies and AGNs. We show this boundary at $z = 1.6$ (thin dotted line), which is consistent with the location of the majority of the FMOS sources. We remove FMOS sources located above this line as AGN candidates, and perform a fit to our sample with the same functional form as Equation (4), yielding

$$\log([\mathrm{O\,III}]/\mathrm{H}\beta) = \frac{0.61}{\log([\mathrm{N\,II}]/\mathrm{H}\alpha) - 0.1336} + 1.081. \quad (5)$$

Here, the coefficient is fixed at the same value (0.61) as the local relation (Equation (4)). The fit is shown as a thick blue line in Figure 4.

The average measurements shown in Figure 5, based on the stacked spectra of Sample-2 in five bins of stellar mass (see Table 2), are consistent with the individual data points and in good agreement with the best-fit relation, thus confirming a clear offset from the local sequence. For local SDSS galaxies, the stacked line ratios in 24 stellar mass bins for $10^{8.9} \leqslant M_*/M_\odot \leqslant 10^{11.3}$ (open squares) and in the same bins as the FMOS sample (green circles) are shown. We note that the local points are slightly off from the ridge line of the contours due to the effects of taking the mean line luminosities (see Section 2.9). At the same stellar mass, the FMOS sample exhibits $[\mathrm{N\,II}]/\mathrm{H}\alpha$ ratios lower than those of local galaxies except for the most massive bin, while having much higher $[\mathrm{O\,III}]/\mathrm{H}\beta$ ratios (>1) over the entire stellar mass range. Salim et al. (2015) find a similar behavior for galaxies with similar stellar masses ($M_* \gtrsim 10^{10}\,M_*$) when comparing local and $z \sim 2$ galaxies. Conversely, in comparison with the sequence of the SDSS stacked points (squares), the FMOS data point in the lowest mass bin ($M_* \sim 10^{9.6-10}\,M_*$) and the low-mass part of the best-fit relation are very close to local loci at low masses ($M_* \sim 10^9\,M_*$; see Section 4 for further discussion). In addition, we note that while the stacked measurements shown in Figure 5 have $\log([\mathrm{O\,III}]/\mathrm{H}\alpha) > 0$, a number of individual FMOS galaxies exist with lower $[\mathrm{O\,III}]/\mathrm{H}\beta$ values that are more consistent with the locus of local massive galaxies in the BPT diagram (Figure 4). Unbiased individual measurements of the line ratios are obviously essential to constrain the lower portion of the sequence of high-z galaxies.

To further assess the robustness of the high-z abundance sequence, we apply a more strict limit on the $[\mathrm{N\,II}]/\mathrm{H}\alpha$ ratio to remove potential AGNs. Following Valentino et al. (2015), we decrease the limit on $\log[\mathrm{N\,II}]/\mathrm{H}\alpha$ from -0.1 (see Section 2.6) to -0.4 (Cid Fernandes et al. 2010). With this restricted sample ($N_{\mathrm{stack}} = 225$), stacked measurements also show a significant offset from the local abundance sequence, thus confirming our results. Therefore, we conclude that the offset of the high-z star-forming population cannot be explained by the effects of AGNs.

The offset in the BPT diagram has been previously reported in our FMOS studies (Zahid et al. 2014b; Kartaltepe et al. 2015) and other works (e.g., Shapley et al. 2005; Erb et al. 2006; Liu et al. 2008; Newman et al. 2014; Cowie et al. 2016) based on stacked and/or individual measurements. Steidel et al. (2014) find an offset using rest-frame UV-selected galaxies at $z \sim 2.3$ from the KBSS-MOSFIRE survey, as

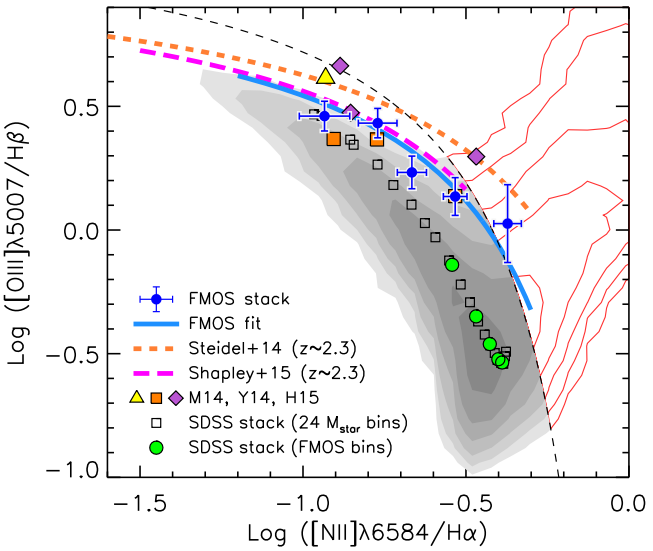

Figure 5. BPT diagram with average measurements. FMOS stacked measurements (Sample-2; blue circles) are shown in five mass bins (with the median value increasing from left to right) with their associated errors. The best-fit relation for the FMOS sample is reproduced from Figure 4 (thick blue line). Shaded and red-line contours indicate local star-forming galaxies and AGNs, classified with the division line of Kauffmann et al. (2003a) (thin dashed line), respectively. For comparison, we show the stacked line ratios of the SDSS star-forming galaxies using the same mass bins as the FMOS sample (green circles) and smaller, equally spaced mass bins (open squares) to illustrate the average locus of the local sample. High-redshift samples are indicated as well (Masters et al. 2014—yellow triangle; Yabe et al. 2014—orange squares; Hayashi et al. 2015—purple diamonds). In addition, the best-fit relations at $z \sim 2.3$ (Steidel et al. 2014—orange short-dashed line; Shapley et al. 2015—magenta long-dashed line) are shown. The FMOS points are in good agreement with the fit to the individual points and indicate an offset of similar magnitude to other studies (see Section 3.1 for comparisons with other studies).

shown in Figure 4 (orange dashed line), which lies above our relation as a whole. Shapley et al. (2015) also confirm the locus of a rest-frame optical selected galaxy sample at $z \sim 2.3$ from the MOSDEF survey (magenta long-dashed line), although it is more similar to our FMOS sample than the KBSS results. The difference between the results from these studies at $z \sim 2$ is likely due to the difference in the adopted sample selection, which results in varying typical ionization and excitation states. The larger offset of the sample of Steidel et al. (2014) may be caused by the selection based on the rest-frame UV emission, which likely leads to higher $[\mathrm{O\,III}]/\mathrm{H}\beta$ ratios (see Section 3.2). Masters et al. (2014) measure the line ratios for highly star-forming galaxies at $z \sim 2$ ($M_* \sim 10^{8.5-9.5}\,M_\odot$), which are consistent with the sample of Steidel et al. (2014), as shown in Figure 5.

At $z \sim 1.5$, three groups provide BPT measurements using Subaru/FMOS, including our program. Yabe et al. (2014) measure the line ratios using the stacked, low-resolution ($R \sim 600$) spectra of star-forming galaxies at $z \sim 1.4$. They use a sample selected on the basis of stellar mass and $\mathrm{H}\alpha$ flux, similar to our study, and thus likely to be representative of the normal star-forming population at this epoch. Their results are in good agreement with our stacked measurements as shown in Figure 5 (orange squares). Hayashi et al. (2015) construct a sample of [O II] $\lambda\lambda$3727, 3729 emitters at $z \sim 1.5$ with an $\mathrm{H}\alpha$ detection with FMOS. Their sample shows a larger offset than those of Yabe et al., Shapley et al., and ours, although it is likely to be more consistent with the sample of Steidel et al. (purple diamonds in Figure 5). The sample of Hayashi et al.

follows an M_*–SFR relation with a slope of 0.38, which is shallower than reported by other studies (∼0.7–0.9, e.g., Kashino et al. 2013; Whitaker et al. 2014). Consequently, the sample is biased toward a population having high specific SFR (sSFR = SFR/M_*) at $\log(M_*/M_\odot) \sim 9$, which is possibly responsible for the high [O III]/Hβ ratios (i.e., a large BPT offset) in their sample. The authors also mention the possibility that their [O II] emitter selection causes such a bias.

After these studies, it remains to be understood whether the offset in the BPT diagram keeps increasing beyond $z \sim 1.5$–2 or saturates. In this respect, it is important to properly account for all possible section biases (see e.g., Cowie et al. 2016). Further investigation of the selection biases and the redshift evolution will be presented in a companion paper (S. Juneau et al. 2017, in preparation). Obviously, the presence of an offset indicates that high-z star-forming galaxies have ionized gas with physical properties dissimilar to those of local galaxies. In Section 4, we discuss several possible origins of the offset of high-z galaxies from the local sequence, including variations in $q_{\rm ion}$, the shape of the UV radiation from the ionizing sources, and gas density (e.g., Masters et al. 2014; Hayashi et al. 2015; Kewley et al. 2015; Shapley et al. 2015; Cowie et al. 2016).

3.2. Mass–Excitation (MEx) Diagram

To further illustrate the magnitude of the [O III]/Hβ offset, we show in Figure 6 the mass–excitation (MEx) diagram (M_* versus [O III]/Hβ). This diagram was introduced by Juneau et al. (2011) to identify galaxies hosting an AGN at intermediate redshifts. Local star-forming galaxies show a decline in the [O III]/Hβ ratio with increasing stellar mass because more massive galaxies are more metal-rich and metal-line cooling becomes more efficient in such systems. In contrast, AGNs present much higher ratios than the star-forming population, especially at $M_* \gtrsim 10^{10}\,M_\odot$ (red contours in Figure 6).

Figure 6 shows the [O III] λ5007/Hβ ratios as a function of M_* for 121 galaxies in our Sample-2 (filled circles). For comparison, local star-forming galaxies are shown by shaded contours, with their median line ratios in stellar mass bins. We highlight the divisions between star-forming galaxies, composite objects, and AGNs, as derived by Juneau et al. (2014) for local galaxies (dashed line). It is clear that FMOS galaxies show higher [O III]/Hβ ratios on average than local galaxies at a fixed stellar mass, and that many individual measurements fall within regions classified as composite objects (between the two dashed lines) or AGNs (above the upper line) although the error bars are typically too large to constrain the true category to which each galaxy belongs. The average measurements, based on the stacked spectra of Sample-2 in five mass bins (see Table 2), confirm a substantial offset toward higher [O III]/Hβ ratios by ∼0.5 dex. In addition, we note that the FMOS sample shows a clear negative correlation between stellar mass and line ratio, similar to local galaxies.

Juneau et al. (2014) also derive the offset of the boundary as a function of the luminosity threshold of the Hα emission line (Equation (B1) of Juneau et al. 2014) to maximize the fraction of objects successfully classified as either star-forming or AGNs. We shift the boundary by $\Delta \log M_* = +0.54$ dex (solid lines in Figure 6), assuming an Hα luminosity limit of $L_{\rm H\alpha} = 10^{42}$ erg s^{-1}, which corresponds to SFR $\sim 10\,M_*$ yr^{-1} for our sample, although the amount of the offset is less constrained at high luminosities ($L_{\rm H\alpha} > 10^{40.7}$ erg s^{-1}; Juneau et al. 2014). The luminosity-adjusted boundary shows a good agreement with our FMOS galaxies. The majority of the FMOS sources fall below the demarcation line and are thus classified as star-forming galaxies, while most of the remaining ones are classified as composite galaxies. At the same time, half of potential AGNs (star and squares in Figure 6) fall within the AGN-dominated region. While our sample is not purely luminosity-limited, it is likely that the luminosity-dependent boundary derived on the basis of local galaxies provides a good classification even for high-redshift galaxies, as originally reported by Juneau et al. (2014). A companion paper further investigates the locus of star-forming galaxies in the BPT and MEx diagrams as a function of the detection limits of emission-line luminosity (S. Juneau et al. 2017, in preparation).

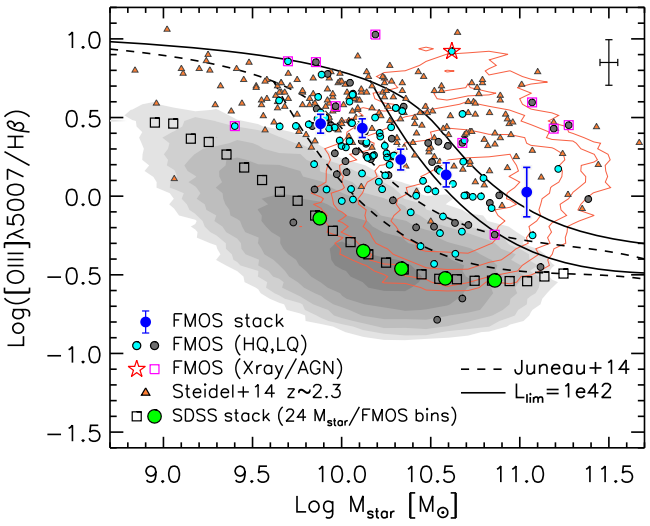

Figure 6. Mass–excitation (MEx) diagram: M_* vs. [O III] λ5007/Hβ. Individual FMOS galaxies are shown with filled circles for two groups: high quality (HQ; cyan) and low- (LQ; gray). Typical error bars of FMOS galaxies are shown in the upper-right corner. AGN candidates are indicated by a star (X-ray-detected source) and magenta squares (others, see Section 2.6). Large blue circles are average measurements of Sample-2 based on the stacked spectra in five mass bins. Contours and symbols, representing the local sample, are the same as in Figure 5. In addition, a sample at $z \sim 2.3$ from Steidel et al. (2014) is shown with orange triangles. Dashed curves indicate a demarcation between star-forming, composite objects, and AGNs, derived by Juneau et al. (2014). The solid lines indicate these same boundaries for a luminosity-limited sample with $L_{\rm H\alpha} > 10^{42}$ erg s^{-1}. Our individual and stacked points show much higher [O III]/Hβ ratios than those of local star-forming galaxies, and agree with the luminosity-adjusted boundary.

We also plot the measurements for $z \sim 2.3$ galaxies from Steidel et al. (2014). They show significantly higher line ratios than local galaxies and even our FMOS sample over the entire stellar mass range. These higher [O III]/Hβ ratios are essentially responsible for the larger offset in the BPT diagram (orange dashed line in Figure 4). These elevated ratios may be due to the redshift evolution of typical conditions (e.g., an enhanced number of hotter stars; see Steidel et al. 2014) and possibly to the UV-bright selection favoring such higher [O III]/Hβ ratios.

3.3. Diagnostics with [S II]/Hα

An alternative BPT diagram compares the line ratios [S II] $\lambda\lambda$6717, 6731/Hα and [O III] λ5007/Hβ to separate the star-forming population from the AGNs (hereafter "[S II]-BPT" diagram; Veilleux & Osterbrock 1987), although it does not provide as clear a division as that based on [N II]/Hα (Kewley et al. 2006; Pérez-Montero & Contini 2009). Contrary to

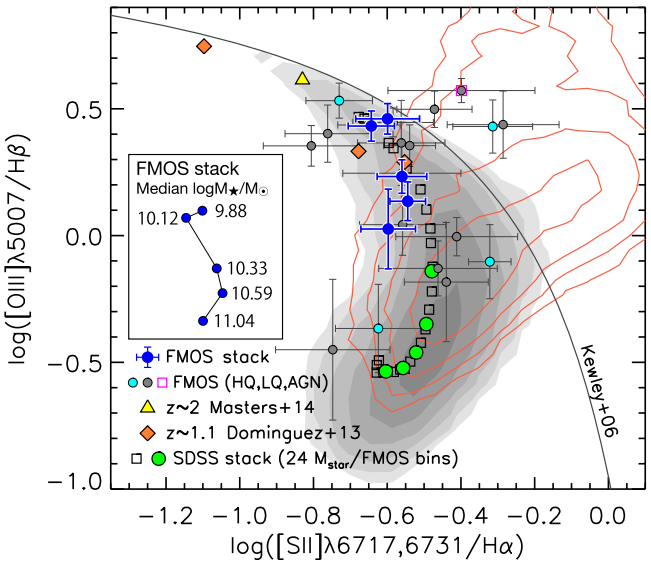

Figure 7. [S II]-BPT diagram: [O III] $\lambda5007/\mathrm{H}\beta$ vs. [S II] $\lambda\lambda6717, 6731/\mathrm{H}\alpha$. The FMOS sample is shown as filled circles for two groups: high quality (HQ; cyan) and low quality (LQ; gray). A magenta square marks an AGN candidate. Large blue circles are stacked points in five mass bins (Sample-2) with the median masses given in the inset box. Data from Domínguez et al. (2013, diamond) and Masters et al. (2014, triangle) are presented. Contours and symbols, representing the local sample, are the same as in Figure 5. A thin solid curve is a demarcation between local star-forming galaxies and AGNs (Kewley et al. 2006). Our FMOS sample shows an offset toward lower [S II]/Hα ratios at a fixed [O III]/Hβ from the local average relation at $M_* \gtrsim 10^{10.5}\,M_\odot$, which suggests an enhancement in $q_{\rm ion}$ in high-z galaxies (see Section 4).

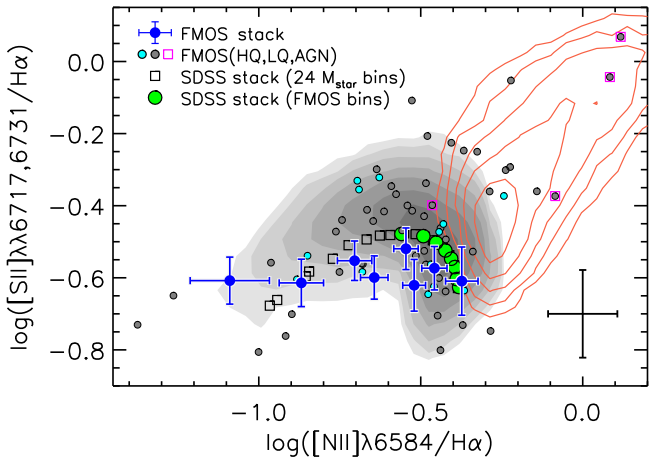

Figure 8. [N II] $\lambda6584/\mathrm{H}\alpha$ vs. [S II] $\lambda\lambda6717, 6731/\mathrm{H}\alpha$. The FMOS sample is shown as filled circles for two groups: high quality (HQ, cyan) and low quality (LQ, gray). Typical error bars are shown in the lower-right corner. Magenta squares mark AGN candidates. The stacked points are based on the spectra of Sample-1 in eight stellar mass bins (large blue circles). Contours and symbols, representing the local sample, are the same as in Figure 5, except that the green circles show the stacked ratios in the eight M_* bins as the FMOS sample. Our sample shows no specific trend between these line ratios, unlike the local sample (see Section 3.3).

offsets seen in the standard BPT diagram at high redshift (Figure 4), no systematic difference of the [S II]-BPT diagram for high-redshift galaxies has been reported (e.g., Domínguez et al. 2013; Masters et al. 2014).

In Figure 7 we show 19 individual galaxies of Sample-2 and the average line ratios based on stacked spectra in five bins of stellar mass (Table 2). Four objects fall within the AGN region, above the classification line derived by Kewley et al. (2006, thin solid line in Figure 7). One of them is identified as an AGN based on the [N II]-BPT plot (magenta square). For comparison, we show the distribution of SDSS galaxies by contours and the stacked line ratios in mass bins (green circles and squares). Similarly to Figure 5, the stacked points are slightly off from the ridge line of the contours. From the individual measurements, the distribution appears to follow that of local star-forming galaxies, although we are hampered by the limited sample size and errors on individual measurements. On the other hand, the FMOS stacked data points indicate a departure toward lower [S II]/Hα ratios compared to average loci of local galaxies (both the ridge line of the contours and the sequence of the stacked points) with increasing stellar mass at $M_* \gtrsim 10^{10.5}\,M_\odot$, while showing a similarity to local galaxies at lower masses. We note that Shapley et al. (2015) find similar [S II]/Hα and [O III]/Hβ ratios, indicative of a shift toward lower [S II]/Hα values at high stellar masses, although the authors do not comment on it. We further discuss the origins of the offset in the [S II]-BPT diagram in Section 4.

An additional diagnostic relation for emission-line galaxies is based on the line ratios [S II] $\lambda\lambda6717, 6731/\mathrm{H}\alpha$ and [N II] $\lambda6584/\mathrm{H}\alpha$. This diagram was first introduced by Sabbadin et al. (1977) to distinguish between planetary nebulae, H II regions, and supernova remnants. In past years, this diagram has also been used to separate star-forming galaxies from AGNs (Lamareille et al. 2009; Lara-López et al. 2010a). In Figure 8, we show 61 FMOS galaxies and average measurements based on the stacked spectra in eight mass bins (Sample-1; Table 2). Individual galaxies are in general agreement with the distribution of local star-forming galaxies (shaded contours). In comparison with the local average points (open squares), the FMOS stacked measurements have slightly lower [S II]/Hα ratios at a given [N II]/Hα with the exception of those at both the highest and lowest masses. The FMOS stacked points occupy a narrow range of $\log[\mathrm{S\,II}]/\mathrm{H}\alpha \sim -0.6$, and have no specific trend with [N II]/Hα or stellar mass, as seen in local galaxies. Our results differ slightly from those of Yabe et al. (2015), which have lower [S II]/Hα ratios over $-1.1 < \log([\mathrm{N\,II}]/\mathrm{H}\alpha) < -0.6$. Finally, we see that there is a minimal contribution from AGNs to our stacked measurements, while a few individual sources are possibly present (see the Appendix for a full assessment on AGNs within our sample).

3.4. Electron Density

The electron density $n_{\rm e}$ can be measured from the intensity ratio [S II] $\lambda6717/$[S II] $\lambda6731$. Here, we convert the [S II] doublet ratio into $n_{\rm e}$ using the TEMDEN routine from the NEBULAR package of STSDAS/IRAF, assuming a fixed electron temperature of $T_{\rm e} = 10^4$ K. While this temperature is commonly assumed for typical H II regions, the electron temperature is sensitive to the gas-phase metallicity and can vary in the range ~5000–20,000 K (e.g., Wink et al. 1983; Andrews & Martini 2013). We note that the temperature dependence of the electron density, derived from [S II] lines, is weak around this choice (maximally $\lesssim$0.2 dex; Copetti et al. 2000). The line ratio is sensitive to the electron density over the range $10 \lesssim n_{\rm e}/\mathrm{cm}^{-3} \lesssim 5 \times 10^3$, while it saturates at upper ([S II] $\lambda6717/$[S II] $\lambda6731 \sim 1.45$) and lower (~0.45) limits for lower and higher electron densities, respectively. The doublet lines are well resolved with the high resolution of FMOS (see Figure 2). Due to the close spacing of these lines in wavelength, the measurements are free from uncertainties in the absolute flux calibration and not impacted by dust

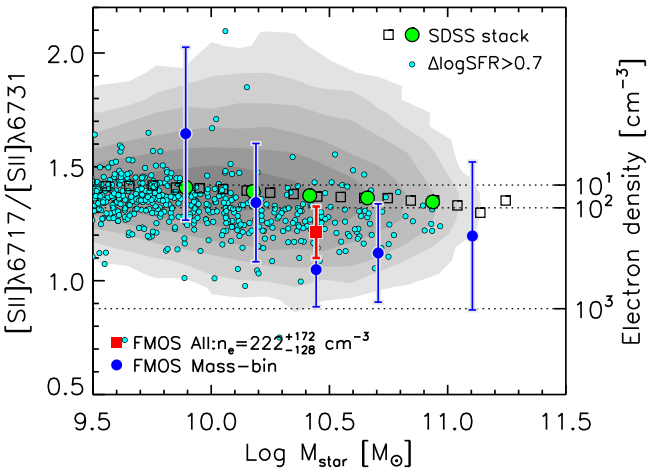

Figure 9. [S II] λ6717/[S II] λ6731 ratio as a function of stellar mass. The corresponding electron densities are given on the right vertical axis and by the horizontal dashed lines ($n_e = 10$, 10^2 and 10^3 cm^{-3}). Blue filled circles indicate average measurements based on the stacked spectra in five bins of stellar mass (Sample-1), and a red square marks the measurement based on the entire sample ($n_e = 222^{+172}_{-128}$ cm^{-3}). Contours and symbols, representing the local sample, are the same as in Figure 5. Cyan circles indicate local sources with an offset from the local star-forming main sequence $\Delta\log(\mathrm{SFR}) \geqslant 0.7$ dex (see Section 3.4).

extinction. However, no single galaxy in the FMOS sample has a significant measurement of the line ratio to constrain the electron density.

In Figure 9, we present the [S II] λ6717/[S II] λ6731 ratios based on the stacked spectra (Sample-1) in five mass bins (blue circles) and based on the entire sample (red square), and the median values of the local sample (squares and green circles). The average electron density of the full sample is $n_e = 222^{+172}_{-128}$ cm^{-3}, which is higher than the average electron density, derived from [S II] lines, in local galaxies as shown in Figure 9 ($n_e = 10$–100 cm^{-3}; Brinchmann et al. 2008). We split the sample into mass bins, but do not find any significant trend with mass due to large uncertainties on our measurements.

Moreover, we compare our measurement with local galaxies having high SFRs that match those of our FMOS sample. We select local star-forming galaxies with $\Delta\log$ SFR > 0.7 dex, where $\Delta\log$ SFR is defined as the difference between the observed SFR and the typical value of main-sequence galaxies at a given stellar mass (Elbaz et al. 2007). Figure 9 shows that such high-SFR local galaxies are biased toward a lower [S II] doublet ratio (i.e., a higher electron density) that is more similar to that of our high-z sample than to that of the entire local sample.

Our result is consistent with findings reported in the literature. For example, Shirazi et al. (2014) find that the electron density of ionized gas in high-z star-forming galaxies ($z \approx 2.4$–3.7) is greater than in matched local galaxies, selected to have the same stellar mass and sSFR. Shimakawa et al. (2015) measure the electron densities of 14 Hα emitters at $z = 2.5$ by the line ratio [O II] λ3729/λ3726, and find a median electron density to be 291 cm^{-3}. Sanders et al. (2016) find a median $n_e = 225^{+119}_{-4}$ cm^{-3} from the [O II] doublet and $n_e = 290^{+88}_{-169}$ cm^{-3} from the [S II] doublet for a sample at $z \sim 2.3$ from the MOSDEF survey. Onodera et al. (2016) find $\sim 10^{2-3}$ cm^{-3} for star-forming galaxies at $z \approx 3.3$. Therefore, we can safely conclude that H II regions in high-z galaxies have an electron density that is 2–10 times higher than that of local galaxies on average.

3.5. The Line Ratio [N II]/[S II]

Kewley & Dopita (2002) investigate the feasibility of using the line ratio [N II] λ6584/[S II] $\lambda\lambda$6717, 6731 as an abundance diagnostic. Sulfur is one of the α-elements, which include, e.g., O, Ne, Si, produced through *primary* nucleosynthesis in massive stars and supplied to the ISM through type-II supernovae. In contrast, nitrogen is generated through both the primary process and a *secondary* process, where ^{12}C and ^{16}O initially contained in stars are converted into ^{14}N via the CNO cycle. Therefore, the [N II]/[S II] ratio is sensitive to the total chemical abundance, particularly in a regime where secondary nitrogen production is predominant, while this ratio is almost constant if most nitrogen has a primary origin (see, e.g., Figure 4 of Kewley & Dopita 2002). The advantage of the use of [N II]/[S II] is that their wavelengths are separated by only $\sim$140 Å, hence they can be observed simultaneously and the line ratio is nearly free from the effect of dust extinction (typically $<$0.03 dex). Here we neglect dust extinction, and define

$$N2S2 = \log([\mathrm{N\,II}]\,\lambda6584/[\mathrm{S\,II}]\,\lambda\lambda6717,\,6731). \quad (6)$$

Figure 10(a) shows the [N II]/[S II] ratio as a function of stellar mass for local star-forming galaxies and for the FMOS sample. The local sample shows a clear correlation between the line ratio and stellar mass above $M_* \sim 10^{9.5} M_\odot$ and reaches $N2S2 \sim 0.3$ at the massive end ($\gtrsim 10^{11}\,M_\odot$), as illustrated by the median points (squares). This tight correlation reflects the regime where secondary nitrogen production is dominant. We find that 61 individual FMOS galaxies with an $N2S2$ measurement show a significant correlation with stellar mass at $>$99% confidence level with a Spearman's rank correlation coefficient $\rho = 0.41$. The trend of these individual measurements is well represented by the stacked measurements based on the co-added spectra of Sample-1 in eight mass bins (blue circles; see Table 2). Therefore, it is likely that the ISM is enriched to a level where nitrogen is dominantly produced by the secondary process for the majority of our sample. The $N2S2$ reaches the same level as in local galaxies at the massive end ($\gtrsim 10^{11} M_\odot$) while, on average, galaxies with $M_* < 10^{11}\,M_\odot$ have lower $N2S2$ values, and thus lower secondary-to-primary elemental abundance ratios, than found in local galaxies at the same stellar mass. This trend is analogous to the mass–metallicity relation as discussed in Section 5.

We note that the [N II]/[S II] ratio is relatively insensitive to the change in $q_{\rm ion}$, although the values of [N II]/Hα and [S II]/Hα depend on $q_{\rm ion}$. According to calculations of photoionization by Dopita et al. (2013, see their Figure 20), the [N II]/[S II] ratio is nearly invariant with $q_{\rm ion}$ over $\log q_{\rm ion}/(\mathrm{cm\ s^{-1}}) \sim 7.0$–$8.5$ at lower ratios ($N2S2 \sim -0.5$; i.e., at lower masses), while the ratio increases maximally by $\lesssim$0.1 dex at higher ratios ($N2S2 \sim 0$; i.e., at high masses) for an increase in $q_{\rm ion}$ by 0.5 dex (from $\log q_{\rm ion}/(\mathrm{cm\ s^{-1}}) = 7.0$ to 7.5). While an enhancement of $q_{\rm ion}$ of $\lesssim$0.5 dex is expected to arise in high-z galaxies (see Section 4), such a weak dependence of $N2S2$ on $q_{\rm ion}$ does not affect the trend seen in Figure 10.

Figure 10(b) compares the line ratios [O III]/Hβ and [N II]/[S II]. The stacked measurements, based on the co-added spectra of Sample-2 in five mass bins, clearly show higher [O III]/Hβ ratios at a given [N II]/[S II] (and vice versa) than in

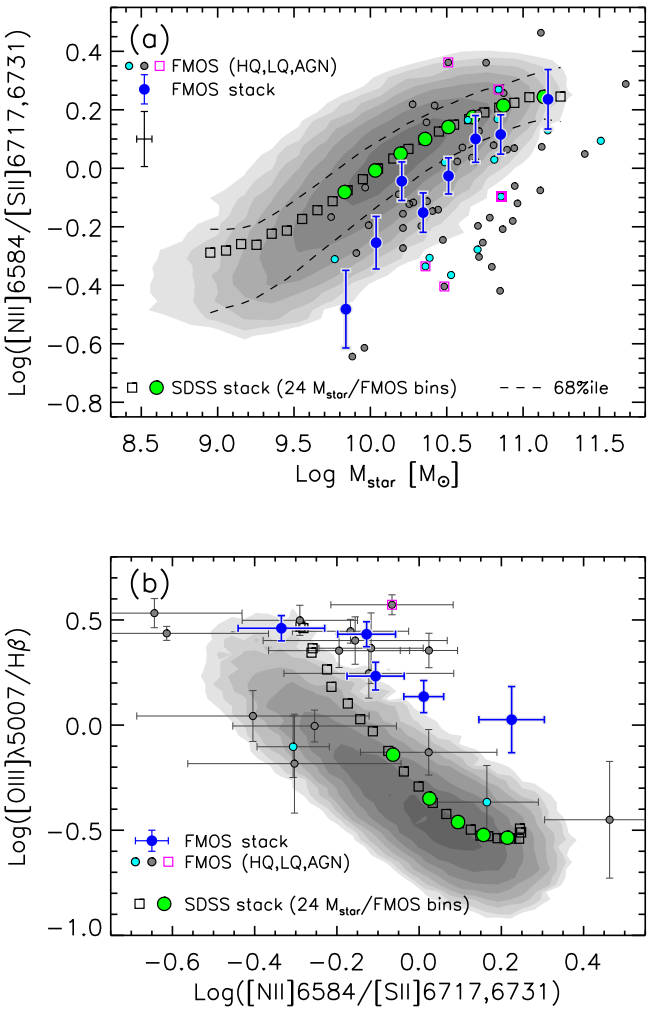

Figure 10. (a) The ratio [N II] λ6584/[S II] $\lambda\lambda$6717, 6731, a proxy for the N/O ratio (and thus the chemical enrichment; see Section 3.5), as a function of stellar mass. The FMOS galaxies are shown with filled circles separately for high-quality (HQ; cyan) and low-quality (LQ; gray) groups. Typical error bars are shown in the upper-left corner. The stacked data points are based on co-added spectra of Sample-1 in eight mass bins (blue circles). (b) [N II] λ6584/[S II] $\lambda\lambda$6717, 6731 vs. [O III] λ5007/Hα. The FMOS galaxies are shown as filled circles. A magenta square indicates an AGN candidate. The average measurements are based on the stacked spectra of Sample-2 in five mass bins (blue circles). The stellar mass increases from left to right. The offset of high-z galaxies to higher [O III]/Hβ at fixed [N II]/[S II] indicates that they have a higher excitation state than local galaxies with a similar degree of chemical enrichment (see Section 3.5). In both panels, contours and symbols, representing the local sample, are the same as in Figure 5, except that the green circles show the values in the eight mass bins in panel (a).

local galaxies. The majority of the individual points also fall above the local relation, in agreement with the stacked data points. This characteristic of high-z star-forming galaxies is very similar to that found in the sample of Shapley et al. (2015) at $z \sim 2.3$. As discussed extensively in the following sections, this fact indicates qualitatively that high-z star-forming galaxies tend to maintain a higher excitation state for their stage of chemical enrichment than local galaxies.

We also highlight that the local SDSS galaxies have [N II]/[S II] ratios that begin to flatten below $\sim 10^{9.5} M_\odot$ (Figure 10(a)). This flattening may arise from the transition between primary and secondary processes being the predominant mechanism. However, it is possible that selection effects, concerning the detection of faint emission lines (i.e., [N II], [S II]), may affect the [N II]/[S II] ratio at lower masses. Further investigation of this feature is beyond the scope of this work.

4. PHYSICAL ORIGIN OF CHANGES IN EMISSION-LINE PROPERTIES

An explanation of the changes in emission-line properties of high-z galaxies is essential for understanding the characteristics of their ionized gas in star-forming regions. In particular, it is important to specify the primary cause(s) of the offset in the BPT diagram, which has been reported by many studies (e.g., Shapley et al. 2005; Erb et al. 2006; Liu et al. 2008; Masters et al. 2014; Newman et al. 2014; Steidel et al. 2014; Yabe et al. 2014; Zahid et al. 2014b; Hayashi et al. 2015; Kartaltepe et al. 2015; Cowie et al. 2016). Several factors have been suggested and discussed, including the metal abundance, ionization parameter, hardness of the EUV radiation field, and gas density (pressure). A higher $q_{\rm ion}$ facilitates the ionization of singly ionized elements to a doubly ionized state, thus increasing the [O III]/Hβ ratio, while decreasing [N II]/Hα and [S II]/Hα (Kewley & Dopita 2002). Alternatively, a harder ionizing radiation field has also been considered as the origin of the BPT offset that causes an increase in the three line ratios given above (Levesque et al. 2010; Kewley et al. 2015). Recently, Steidel et al. (2016) suggested the presence of harder stellar spectra due to the existence of massive, metal-poor binary systems. In addition, a higher H II gas density will increase the three line ratios because of the higher rate of collisional excitation of metal ions. As a result, the BPT abundance sequence will be shifted toward the upper right (e.g., Brinchmann et al. 2008). Kewley et al. (2013a) summarize the effects of varying ISM properties on the star-forming locus in the BPT diagram.

4.1. Comparison with Theoretical Models

We aim to determine the impact of each physical effect on changes in the location of high-z galaxies in emission-line diagrams by comparing our observational data with theoretical models. We use the photoionization code MAPPINGS V.[24] In Figure 11, we make use of a new diagnostic tool, recently proposed by Dopita et al. (2016), using combinations of [N II] λ6584/Hα, [N II] λ6584/[S II] $\lambda\lambda$ 6717, 6731, and [O III] λ5007/Hβ to clearly separate the dependence on metallicity (Z) from that on the ionization parameter ($U = q_{\rm ion}/c$) at a given gas pressure (P) (see Figure 2 of Dopita et al. 2016). The line ratios are computed as functions of U and Z at gas pressures of $\log P/k = 5.2$ or 6.2 cm^{-3} K. In Figure 12, we compare the local and high-z line ratios with the model grids in (a) the [N II]/[S II] versus [O III]/Hβ, (b) the [S II]-BPT, and (c) the BPT diagrams. In each panel, we consider the individual physical effects that can be responsible for the differences in line ratios between low-z and high-z galaxies at a given stellar mass. The paths of the line ratios from low z to high z due to different physical factors are schematically illustrated by various arrows. In each diagram in Figure 12, their direction and magnitude are prescribed based on the model grid by comparing the loci, i.e., the coordinates ($\log$(O/H), $\log U$), of the stacked data points at both epochs in the same mass bins (low z—green; high z—blue circles). Although the theoretical calculations do not fully reproduce the observed line ratios with

[24] https://miocene.anu.edu.au/mappings

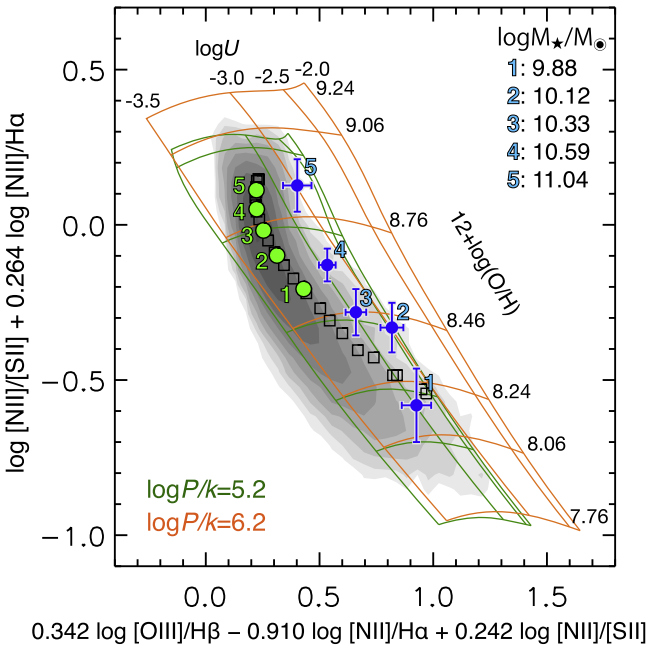

Figure 11. Comparison of combinations of line ratios, as presented in Figure 2 of Dopita et al. (2016), with theoretical model grids (MAPPINGS V) for varying metallicity Z ($12 + \log(\mathrm{O/H})$), ionization parameter ($U = q_{\rm ion}/c$), and gas pressure (P). Average measurements of the FMOS sample are based on stacked spectra in five stellar mass bins (Sample-2; blue circles, labeled as #1–5). The median M_* are given in the upper-right corner. Shaded contours show local star-forming galaxies, with their stacked points in 24 equally spaced mass bins ($10^{8.9} \leqslant M_*/M_\odot \leqslant 10^{11.3}$; squares) and in the same five mass bins as the FMOS sample (green circles, labeled as #1–5). Based on the theoretical model grids, our FMOS sample shows a ∼0.3–0.4 dex enhancement in $q_{\rm ion}$ as compared to local galaxies over the entire stellar mass range.

precision, they do provide qualitative insight into the relation between the line ratios and physical parameters. In the following subsections, we describe the effects of each physical factor in detail.

4.1.1. Metallicity

First, we consider the changes in line ratios due to changes in metallicity. In Figure 11, a comparison between the local and our FMOS samples shows that high-z galaxies have the same metallicity (y-axis) as the local sample at the massive end ($M_* > 10^{10.8}\,M_\odot$), while metallicities of lower-mass galaxies are lower than those of local galaxies of the same stellar mass.[25] Such a decline in Z for high-z galaxies with $M_* \lesssim 10^{10.8}\,M_\odot$ (binned data labelled as #1–4 in the panel) contributes significantly to changes in line ratios. In Figure 12, shifts, corresponding to a decline in Z, are shown by thin blue arrows (pointing in the direction of decreasing Z) while the ionization parameter is fixed. It is evident that a decrease in metallicity does not move galaxies toward high-z loci, hence we conclude that metallicity cannot be the primary cause of the offset between local galaxies and our high-z galaxies.

4.1.2. Ionization Parameter

We investigate the hypothesis that the ionization parameter is higher in star-forming galaxies at high redshifts than in those at low redshift. As shown in the MEx diagram (Figure 6), high-z galaxies have elevated [O III]/Hβ ratios as compared to local galaxies over the full range of stellar mass. Higher [O III]/Hβ ratios are also seen at a given stage of chemical enrichment, as indicated by [N II]/[S II] (Figure 10(b)). These higher [O III]/Hβ ratios can be produced by a higher $q_{\rm ion}$. Evidence of an enhancement in $q_{\rm ion}$ comes from a shift toward lower [S II]/Hβ in the [S II]-BPT diagram (Figure 7); a higher $q_{\rm ion}$ leads to the ionization of $S^+ \rightarrow S^{++}$, which decreases [S II]/Hα. Therefore, an increase in $q_{\rm ion}$ likely plays an important role in causing the offset in the BPT diagram.

In Figure 11, we see an indication, based on a comparison with theoretical models, that our FMOS galaxies have ionization parameters $\log q_{\rm ion}/c \sim -3$, approximately 0.3–0.4 dex higher, on average, than that of local galaxies of the same stellar mass, even if a higher gas pressure is considered. This is consistent with previous studies (e.g., Nakajima & Ouchi 2014; Shirazi et al. 2014; Hayashi et al. 2015; Onodera et al. 2016). Figure 11 also suggests that the FMOS galaxies have higher $q_{\rm ion}$ than local galaxies at fixed metallicity, except for the lowest mass bin (labelled as #1), which shows a level of ionization parameter similar to the low-mass local galaxies ($M_* \sim 10^9\,M_\odot$).

To evaluate the effects of varying $q_{\rm ion}$ on emission-line ratios, it is important to consider the anticorrelation between $q_{\rm ion}$ and Z seen in local galaxies at lower stellar masses ($\lesssim 10^{10}\,M_\odot$) (e.g., Dopita et al. 2000; Kojima et al. 2016). Based on model grids, the local average measurements (squares) show an increase of $q_{\rm ion}$ with decreasing Z at $12 + \log(\mathrm{O/H}) \lesssim 8.6$ (Figures 12(a), (c)). Following a change in line ratios due to Z, we show in Figure 12 a shift corresponding to a change in $q_{\rm ion}$ due to the local $q_{\rm ion}$–Z anticorrelation (narrow red arrows), with a magnitude set to match the local relation at a given metallicity (squares). There is no shift for the two highest mass bins (circles labelled as #4–5) due to small or no change in metallicity. It is clear that these changes in $q_{\rm ion}$ accompanying the metallicity evolution are not fully responsible for the offsets of high-z galaxies. The remaining offsets evidently require a further enhancement in $q_{\rm ion}$ (thick red arrows), which moves galaxies toward higher [O III]/Hβ and constitutes the most important origin of the offset. However, the size of this increase in $q_{\rm ion}$ cannot be fully constrained because other effects may also cause an additional shift in a similar direction (see the following subsection). Here the thick red arrow corresponds to a scaling-up of about 0.3 dex at fixed O/H for all mass bins except the lowest one (#1), as estimated from Figure 11. The contribution from this additional $q_{\rm ion}$ excess seems to be relatively more important for higher mass bins. In contrast, we note that, for the lowest mass bin (labelled as #1), the entire enhancement in $q_{\rm ion}$ could be explained by that coincident with the change in metallicity (i.e., due to the local $q_{\rm ion}$–Z anticorrelation), and thus it does not need the additional excess.

In panel (b), the shift toward both lower [S II]/Hα and higher [O III]/Hβ due to higher $q_{\rm ion}$ is clearly shown, especially in the most massive bin; it is apparent that the only factor that can produce a shift toward the left is an enhancement in $q_{\rm ion}$. Over the stellar mass range of the FMOS sample, the magnitude of the shift is not fully accounted for by just the enhancement of $q_{\rm ion}$ that is expected from the $q_{\rm ion}$–Z relation (narrow red arrows). Therefore, an additional enhancement of the ionization parameter is required to fully produce the offset of high-z galaxies in the emission-line diagrams (thick red arrows).

[25] We further investigate the mass–metallicity relation of our sample based on the [N II]/Hα ratio and the theoretical calibration from Dopita et al. (2016) in Section 5.

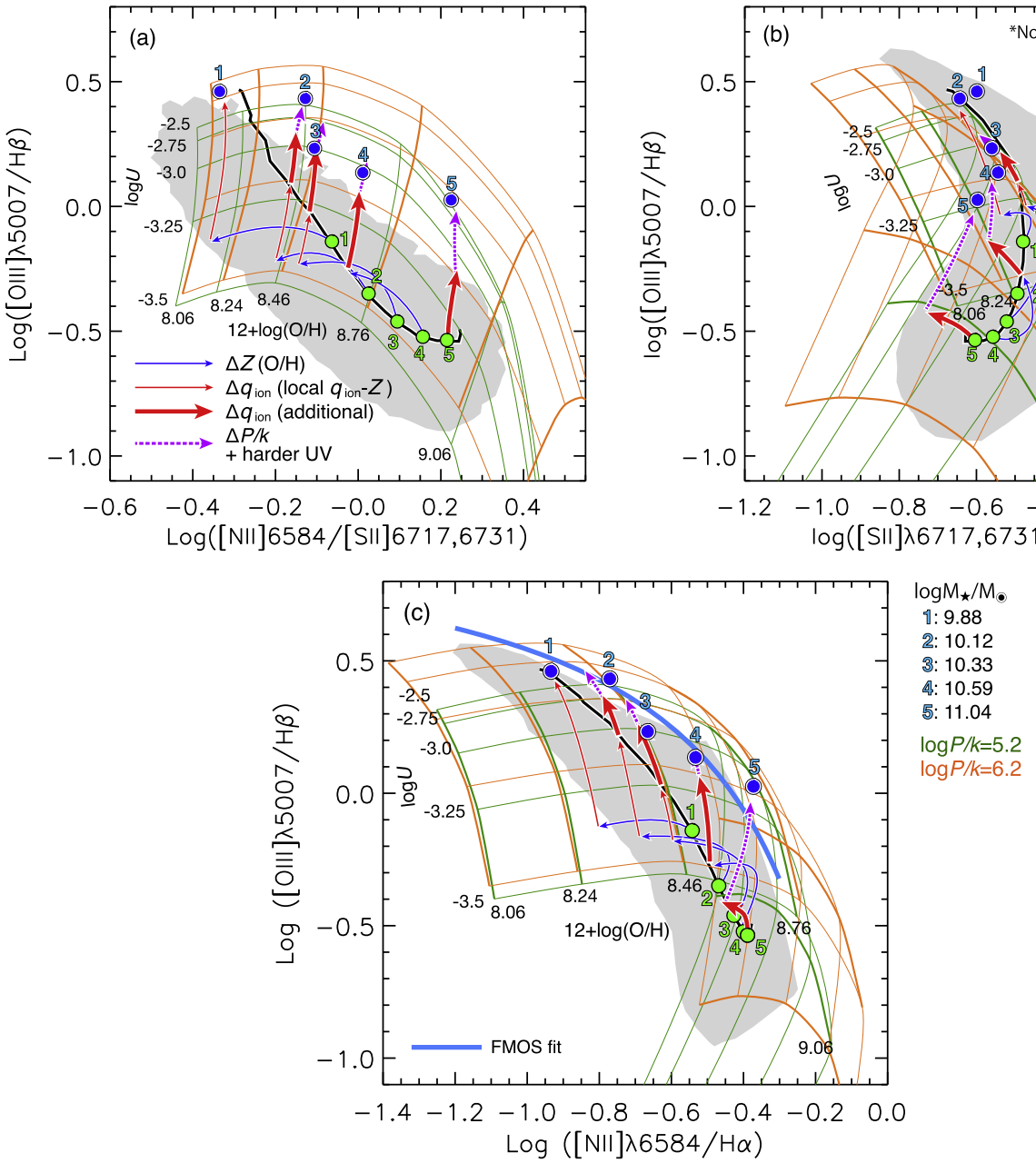

Figure 12. Illustration of the magnitude of effects produced by changes in each physical factor in (a) the [N II]/[S II] vs. [O III]/Hβ, (b) the [S II]-BPT, and (c) the BPT diagrams. The average data points of our FMOS and local samples, and the theoretical model are the same as in Figure 11 except that the sequence of the stacked points in 24 M_* bins (squares in Figure 11) is simply expressed by a black solid line. The median M_* and the gas pressures of the models are shown outside the frame. Arrows indicate corresponding changes in the line ratios for the each factor separately (thin blue arrows—decreases in metallicity; thin red arrows—enhancement of $q_{\rm ion}$ due to the local $q_{\rm ion}$–Z anticorrelation; thick red arrows—excessive enhancement of $q_{\rm ion}$; dotted magenta arrows—remaining effects possibly attributed to high gas pressure and harder radiation field). A shaded region indicates an outline of the distribution of local star-forming galaxies.

4.1.3. Additional Effects (ISM Gas Density and Hardness of the Radiation Field)

While a higher [O III]/Hβ ratio likely indicates an enhancement of $q_{\rm ion}$, additional factors may contribute to higher ratios since [O III]/Hβ increases with a higher gas density and a harder ionizing radiation field. The significance of these additional effects is shown in the [S II]-BPT diagram (Figure 12(b)). While a higher $q_{\rm ion}$ will shift the line ratios toward the upper left (as illustrated by the thick red arrows, mass bins #4 and #5 in particular), an additional offset toward the upper right is needed (as highlighted by the magenta dotted arrows) to match the line ratios of high-z galaxies. We attribute the latter effect to a higher gas pressure, supported by the measurements indicative of a higher electron density (see Section 3.4), as demonstrated by the model grids of different P/k. However, Figure 12 suggests that the remaining shift in line ratios (in particular, the most massive bin labelled as #5) is unlikely to be fully explained even by a gas pressure that is ten times higher. Hence we surmise that there may be additional help from a harder ionizing radiation field to fully match the offset, although the current data cannot ascertain the size of such a contribution. Here, for mass bins #2 and #3, we indicate a shift corresponding to about ten times higher P/k, as expected from the higher electron density we measure (Section 3.4). Meanwhile, there is no additional shift required

for the lowest mass bin (#1) because its line-ratio offset can fully explained by the $q_{\rm ion}$ excess due to the lower O/H (see the previous subsection). We note that it is challenging to quantitatively distinguish the contributions from a higher $q_{\rm ion}$ (red thick arrows) and from additional factors (magenta dotted arrows), especially at lower stellar masses, because the directions of changes in emission-line ratios are roughly similar for different physical effects. In addition, we caution the reader that the model line ratios and arrows in Figure 12 may be affected by systematic uncertainties.

To conclude, we find that it is likely that all three factors contribute to changes in the emission-line ratios at high redshift. Based on our observations and comparisons with the models, we argue that the emission-line properties of high-z galaxies are a result of the following: (1) a higher $q_{\rm ion}$ than local galaxies of the same stellar mass, with an enhancement in $q_{\rm ion}$ being higher than expected from the $q_{\rm ion}$–Z anticorrelation seen in local galaxies, (2) higher gas density (pressure), and (3) an additional effect possibly attributed to a hardening of the ionizing radiation field. While arguing for the existence of multiple effects, we conclude that an elevation of the ionization parameter *at fixed metallicity* is the dominant factor influencing the emission-line ratios of high-z galaxies. In addition, we highlight that the emission-line ratios of FMOS galaxies in the lowest mass bin ($M_* \sim 10^{9.6-10}\,M_\odot$) can be explained by just the enhancement in $q_{\rm ion}$ accompanying the change in metallicity without invoking additional effects. These facts likely indicate that the excitation properties of the ISM in such low-mass high-z galaxies can be commonly seen in local galaxies with masses about ten times lower ($M_* \sim 10^9\,M_\odot$), while the situation in higher-mass high-z galaxies ($M_* > 10^{10}\,M_\odot$) is dissimilar from that in ordinary local galaxies at any stellar mass.

4.2. What Causes an Enhancement of Ionization Parameter?

Following the above discussion, we consider how the characteristics of H II regions in high-z star-forming galaxies are different from those in local galaxies. If a fixed inner radius of an ionized gas sphere is assumed, the ionization parameter is inversely proportional to the gas density. With the higher gas density of our sample (Section 3.4), a higher $q_{\rm ion}$ requires an increase in the production rate of ionizing photons. An enhancement of the ionizing photon flux in individual H II regions could be simply expected to occur when a larger number of stars form in each gas cloud than in local galaxies (Kewley et al. 2015). This corresponds to a higher star formation efficiency (SFE), such that SFR = SFE $\times$ $M_{\rm gas}$ (where $M_{\rm gas}$ is the mass of molecular gas), and indeed the SFE is higher at higher redshift (e.g., Genzel et al. 2015). Furthermore, a higher ionizing photon flux could also arise due to harder stellar spectra, which induce additional changes in line ratios, as discussed above (Section 4.1.3). A hardening of the overall stellar radiation field could result from a top-heavy IMF that increases the proportion of hot massive stars, from a metal-poor stellar population (see, e.g., Levesque et al. 2010), or from massive binaries, which have a lifetime on the main sequence that is longer than that of single stars (see Steidel et al. 2016, and references therein). Steidel et al. (2016) suggest that, at high redshifts, the stellar atmospheres of ionizing massive stars have a lower Fe/O abundance ratio than the solar value, as a result of chemical enrichment being dominated by Type II supernovae. Since the photospheric line blanketing is mainly due to iron, the Fe depletion results in a lower opacity for ionizing photons at fixed O/H, thus leading to a higher ionizing parameter and/or harder ionizing radiation field for the circumstellar environment. Examination of these various possible origins requires not only measurement of the ISM properties, but also further understanding of the properties of the stellar component, for which very deep spectroscopy in optical (rest-frame UV) is especially important.

The geometrical properties of gas clouds and star-forming regions could also affect the physical properties of the ionized gas, and thus the emission-line ratios. Given high sSFRs of high-z galaxies, it is considered likely that an H II region is close to, or overlapping, another ionized gas region. In such cases, ionizing photons from adjacent H II regions effectively increase $q_{\rm ion}$. The model photoionization calculations used above assume an "ionization-bounded" H II region, for which the radius is determined by the ionization equilibrium (Stömgren radius). In contrast, "density-bounded" H II regions are entirely ionized and have a radius determined by the size of the gas cloud. In such a situation, the sizes of a singly ionized (i.e., [N II], [S II]) region and the hydrogen recombination region are smaller than in the ionization-bounded cases, while the doubly ionized region (i.e., [O III]) is less affected. As a consequence, the [O III]/Hβ ratio will increase, while the [N II]/Hα and [S II]/Hα ratios decrease, as compared with the ionization-bounded case. These changes in the line ratios will be interpreted as a result of an enhancement of $q_{\rm ion}$ (e.g., Kewley et al. 2013a; Nakajima & Ouchi 2014). However, it remains completely unclear how common density-bounded H II regions are in both local and higher-redshift star-forming galaxies.

Alternatively, we consider the effects from low-density ($\sim$0.1 cm^{-3}) diffuse ionized gas (DIG) in galaxies, which is widely distributed in interstellar space and is ionized by radiation from hot massive stars (e.g., Reynolds 1984, 1992; Domgorgen & Mathis 1994). In a galaxy-wide spectrum, the nebular emission consists of the combination of emission from individual H II regions and the DIG component. The DIG is known to have a very low $q_{\rm ion}$, as compared to denser H II regions, as indicated by weak [O III] lines (Domgorgen & Mathis 1994). Therefore, the contribution from DIG may decrease the effective value of $q_{\rm ion}$ estimated from the galaxy-wide flux, although such effects are not yet well understood. Low-z galaxies could be expected to make a larger DIG contribution to the integrated flux than high-z galaxies, which may be more similar to pure H II regions owing to their high SFRs. We test the hypothesis that the changes in the emission-line ratios are caused by the change in the DIG contribution to the galaxy-wide emission. In Figure 13, our FMOS galaxies are compared with individual H II regions in local spiral galaxies (van Zee et al. 1998). The data points of H II regions trace well the BPT abundance sequence of local galaxies based on the galaxy-wide spectra, and thus the offset of our FMOS galaxies remains even in comparison with pure H II regions. This apparently means that a contribution from DIG does not explain the changes in the observed emission-line ratios between local and high-z galaxies, thus rejecting the above working hypothesis.

4.3. Enhancement of N/O

Previous studies have reported a lack of any significant offset between local and high-z galaxies in the [S II]-BPT diagram as an indication that the offset in the BPT diagram is caused by an effect other than a higher $q_{\rm ion}$ or a higher ionizing radiation

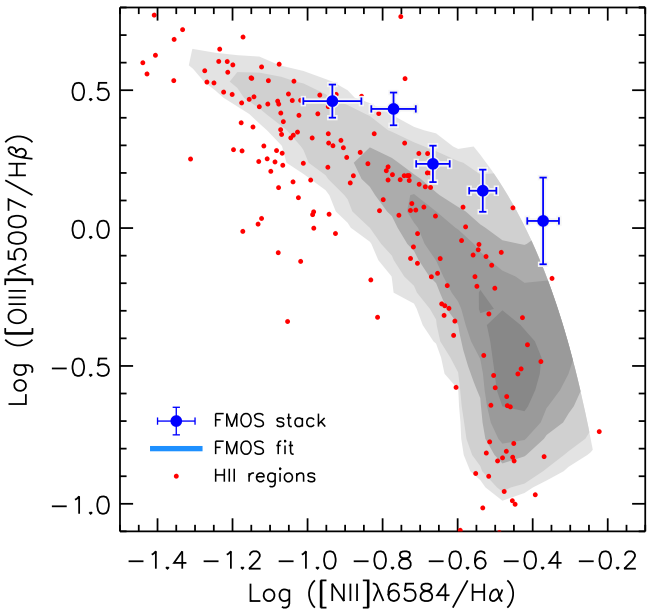

Figure 13. Comparison of line ratios (BPT diagram) for FMOS galaxies (average values as in Figure 5) and local H II regions (van Zee et al. 1998; red circles). Local star-forming galaxies are shown by gray contours.

field (Masters et al. 2014; Shapley et al. 2015). An elevated nitrogen-to-oxygen (N/O) abundance ratio at a given O/H has been suggested as such a possible cause of the BPT offset toward higher [N II]/Hα at a fixed [O III]/Hβ (e.g., Masters et al. 2014, 2016; Steidel et al. 2014; Shapley et al. 2015; Yabe et al. 2015; Cowie et al. 2016; Sanders et al. 2016). In contrast to these studies, we find an offset in the [S II]-BPT diagram and explain the emission-line ratios of high-z galaxies without invoking a change in the N/O–O/H relation. A quantitative constraint would require a metallicity determination that is independent of the N abundance (e.g., direct T_e or R_{23} index) and a reliable measurement of N/O for high-z galaxies. While such studies are not feasible with the primary FMOS spectroscopic sample, future [O II] $\lambda\lambda$3726, 3729 follow-up observations will permit us to investigate these issues further.

We highlight a recent study by Steidel et al. (2016) that finds by using a composite spectrum of $z \sim 2.4$ galaxies that an average N/O and T_e-based O/H are in excellent agreement with the N/O–O/H relation of local extragalactic H II regions (Pilyugin et al. 2012). Therefore, it is conceivable that an enhancement of N/O is not the main factor causing the BPT offset at high redshifts. However, we caution that the N/O ratio measured by Steidel et al. (2016) is higher at fixed O/H when compared to a "galaxy-wide" relation derived by Andrews & Martini (2013). Therefore, it still remains unsettled whether the N/O–O/H relation evolves with redshift or not, though to some extent it should, given the different timescales of nitrogen and oxygen release by stellar nucleosynthesis.

5. REVISITING THE MASS–METALLICITY RELATION

We previously reported on the MZ relation based on our FMOS program (Zahid et al. 2014b) using a smaller subset of galaxies (162) than presented in this work. Our MZ relation indicated that the most massive galaxies at $z \sim 1.6$ are fully mature, similar to local massive galaxies, while the lower-mass galaxies are less enriched than local galaxies at a fixed stellar mass. Here, we revisit the MZ relation using a sample four times larger than presented in Zahid et al. (2014b). In particular, the number of massive ($M_* > 10^{11}\,M_\odot$) galaxies in the sample is larger by an order of magnitude.

5.1. Empirical Metallicity Determination Using [N II]/Hα

We use the [N II]/Hα ratio to evaluate the gas-phase metallicity, i.e., the oxygen abundance, 12 + log(O/H). The advantage of using this ratio is the close spectral proximity of the lines, and thus no correction for extinction is required. The high-resolution mode of FMOS cleanly separates the two lines. However, the [N II]/Hα ratio is sensitive to the ionization parameter and hardness of the ionizing radiation field. A 0.5 dex increase in $q_{\rm ion}$ produces a decrease in [N II]/Hα, thus leading to a ~0.4 dex underestimate of metallicity (Kewley & Dopita 2002). Furthermore, metallicities based on the [N II] line depend on the relation between the N/O and O/H ratios. Any empirically or theoretically calibrated metallicity indicator involving a nitrogen line implicitly rests on the assumption of a universal (locally calibrated) relation between N/O and O/H. However, the universality of the relation is still under debate at both low and high redshifts. For instance, the accretion of a substantial amount of metal-poor gas could reduce a galaxy's O/H while leaving its N/O largely unchanged, causing a deviation from the local relation (see Kashino et al. 2016; Masters et al. 2016). Indeed, an enhancement of N/O at fixed O/H has been advocated to explain the offset in the BPT diagram of high-z galaxies (see Section 4.3), although we do not invoke the change in the N/O versus O/H relation as an explanation for the emission-line properties of high-z galaxies (see also Dopita et al. 2016). It is clear that a direct calibration of the relation between N/O and O/H is required to improve upon metallicity determinations of high-z galaxies.

With these caveats in mind, we estimate the metallicities of both local galaxies and the FMOS sample based on a locally calibrated relation. The line ratio is converted to metallicity as given in Maiolino et al. (2008):

$$N2 = -0.7732 + 1.2357x - 0.2811x^2 - 0.7201x^3 - 0.3330x^4 \quad (7)$$

where $N2 = \log([\mathrm{N\,II}]\lambda6584/\mathrm{H}\alpha)$ and $x = 12 + \log(\mathrm{O/H}) - 8.69$. This relation is nearly linear over the metallicity range of interest ($8 < 12 + \log(\mathrm{O/H}) < 9$). On the other hand, the line ratio begins to saturate at higher metallicity (above $N2 \sim -0.3$) as a result of efficient metal cooling, which leads to a decrease in the collisional excitation rate of N^+ (Osterbrock & Ferland 2006).

Figure 14(a) shows the [N II] λ6584/Hα ratios as a function of stellar mass. We plot 436 galaxies with Hα and [N II] detections (Sample-1). The FMOS sample has a broad distribution of [N II]/Hα that spans much of the SDSS locus (see also Zahid et al. 2014b). Many galaxies with less secure measurements ($1.5 < \mathrm{S/N([N\,II])} < 3$) have a low $N2$. This is expected because the [N II] line is generally much weaker than Hα and difficult to detect with FMOS for a reasonable amount of integration time (~a few hours). It is also shown that 54 galaxies have $N2 > -0.2$ (12% of sources with an $N2$ measurement). The locus of such a population is in agreement with the distribution of the local AGNs (red contours in Figure 14(a)). In contrast, roughly half of the X-ray-detected FMOS sources are located at $N2 < -0.2$, consistent with local star-forming galaxies, while the others show higher $N2$ values, especially at high masses. This suggests that AGNs are present

in our sample if there is no prior exclusion, especially at high masses (Mancini et al. 2015), and that the availability of the X-ray observations is important for constructing a sample of pure star-forming galaxies.

To overcome the low S/N of individual detections of the [N II] line, we measure the average [N II]/Hα ratios from the stacked spectra of Sample-1 split into eight bins of stellar mass (see Table 2; blue circles in Figures 14(a), (b)). The stacked points show a clear trend with stellar mass, lying below the average of the individual sources with a detection (Figure 14(a)). Co-adding spectra reduces the bias with respect to detecting the [N II] line since galaxies are identified only by the presence of an Hα detection. In Figure 14(b), the metallicities converted from the stacked [N II]/Hα ratios are shown; they are consistent with the previous measurements from Zahid et al. (2014b, gray triangles). For local galaxies, we show the stacked data points in 24 equally spaced mass bins (squares) and in the same bins as the FMOS sample (green circles). Both the local and FMOS samples are well fit with a model by Zahid et al. (2014a). The model fit and the interpretations are fully described in Section 5.3. Our data show a level of metallicity similar to local galaxies at the massive end ($M_* > 10^{11}\,M_\odot$), while the average measurements in less massive galaxies are lower than those in local galaxies. The difference in metallicity between the local and FMOS samples increases as the stellar mass decreases. Such a behavior of the MZ relation is consistent with an evolutionary scenario, so-called "downsizing" (e.g., Maiolino et al. 2008), where massive galaxies form earlier, and are thus chemically mature at high redshift, while lower-mass systems evolve more slowly.

As described in Section 2.6, we remove galaxies identified as AGNs on the basis of X-ray detection, the BPT diagram (or $N2 > -0.1$ if no [O III]/Hβ measurement is available), or FWHM >1000 km s^{-1}. We further assess the effects of excluding potential AGNs by their [N II]/Hα values, particularly at the massive end. With an upper limit on $N2$ decreased from -0.1 to -0.3, the stacked measurements are still consistent with local massive galaxies, although the values are lower by $\Delta \log(\mathrm{O/H}) \sim 0.15$. Therefore, we conclude that the effects of AGNs do not impact our measurement of the MZ relation at $z \sim 1.6$.

In Figure 14(b), we also show MZ relations based on [N II]/Hα from the literature at $z \sim 1.4$–2.3 (Erb et al. 2006; Steidel et al. 2014; Yabe et al. 2014), which are converted here to a Salpeter IMF and the metallicity calibration of Maiolino et al. (2008). Our measurement is nearly in agreement with Yabe et al. (2014), which is based on a low-resolution FMOS program. The MZ relations at $z \sim 2$ seem to indicate a further decline in metallicity as compared to our relation at $z \sim 1.6$. In addition, the slope seems to be shallower than that of our measurement at $z \sim 1.6$ (see Section 5.3).

Given the sensitivity of the [N II]/Hα ratio to ionization parameter, gas pressure, N/O, and hardness of the ionizing radiation field, some caution is advised when interpreting the shifts seen between the low-z and high-z samples in Figure 14(b) as being due purely to changes in metallicity. Cowie et al. (2016) find that the [N II]/Hα versus O/H relation depends weakly on Hβ luminosity. The luminosity-adjusted relation for the typical $\log L(\mathrm{H}\beta)/(\mathrm{erg\ s^{-1}}) \sim 41.5$–42 of our sample reduces the difference between the MZ relations at $z \sim 0$ and $z \sim 1.6$ by $\sim$0.15–0.2 dex. Despite that, the metallicities of high-z galaxies with $M_* \sim 10^{10}\,M_\odot$ are still smaller than those of local galaxies. We recognize that there may be systematic biases between the metallicity determinations of different samples at these two epochs. However, we use locally and/or theoretically calibrated metallicity indicators

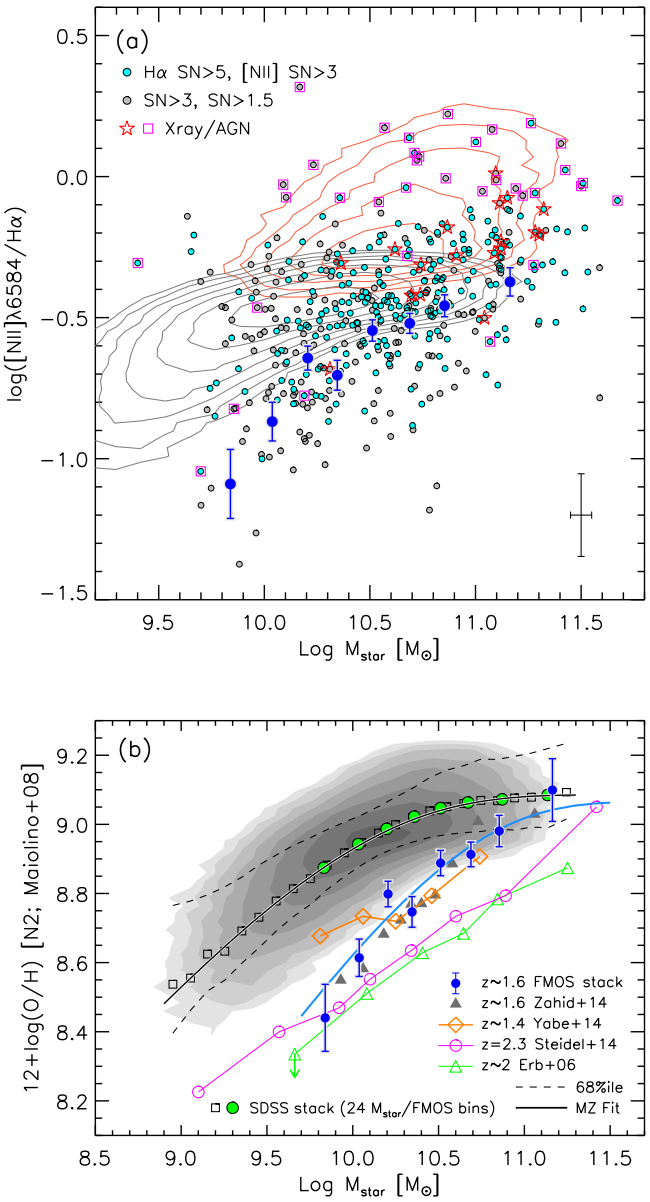

Figure 14. Mass–metallicity relation. (a) [N II]/Hα as a function of stellar mass. Individual FMOS galaxies are shown with the quality of measurement as labelled (cyan—S/N(Hα) > 5 and S/N([N II]) > 3; gray—S/N(Hα) > 3 and S/N([N II]) > 1.5). Typical error bars are shown in the lower-right corner. AGN candidates are highlighted by stars (X-ray detected sources) and magenta squares (others). Contours show the distribution of the local star-forming galaxies (gray) and AGNs (red). The stacked points in the eight M_* bins (Sample-1) are shown by blue filled circles, for which AGNs are removed. (b) Mass–metallicity relation. The oxygen abundance is calculated from the average [N II]/Hα ratio with Equation (7). The FMOS stacked points are the same as in (a) (filled circles). Filled triangles indicate our previous measurement from Zahid et al. (2014b). Empty symbols show the measurements in the literature as labelled. Shaded contours show local star-forming galaxies with the stacked data points in 24 equally spaced mass bins (squares) or in the same eight bins as the FMOS sample (green circles). Dashed lines indicate the central 68th percentile of the local SDSS galaxies. Solid curves show the best-fit relations parameterized in Equation (9), for the FMOS (blue) and local (black) samples.

without any specific correction for high redshift for the remainder of this study.

5.2. New Calibration with [N II]/[S II]

Recently, Dopita et al. (2016) have introduced a new metallicity calibration using both the line ratios [N II]/Hα and [N II]/[S II] that is almost independent of the ionization parameter and gas pressure, as described in Section 4 (see Figure 11). This calibration is effective over the metallicity range $8 < 12 + \log(\mathrm{O/H}) < 9$, and is expressed as follows:

$$12 + \log(\mathrm{O/H}) = 8.77 + N2S2 + 0.264N2, \quad (8)$$

where $N2S2$ is defined by Equation (6). Inclusion of the [N II]/[S II] term ($N2S2$) in the determination of the metallicity provides an assessment of how nucleosynthesis has proceeded through the ratio of secondary to primary elements. This metallicity indicator assumes a relation between the N/O (≈N/S) ratio and the O/H ratio based on a set of local sources (see Figure 1 of Dopita et al. 2016). The authors argue that changes in the N/O ratio at a fixed O/H are not required to explain the emission-line properties of high-z galaxies. However, it is not proven whether such a relation between N/O and O/H is universal, and hence applicable at higher redshfits (or even for local galaxies other than those used for the calibration). This calibration also assumes a one-to-one relation between N/S and N/O, i.e., a constant S/O ratio. We note that the variation in S/O is expected to be small (∼0.1 dex), and indeed the S/O ratio is almost independent of metallicity (Izotov et al. 2006), which supports the use of the [N II]/[S II] ratio as a proxy for the N/O ratio (Pérez-Montero & Contini 2009).

With these considerations and caveats in mind, we present in Figure 15 the MZ relation with metallicity determined from Equation (8) for both local galaxies and our FMOS galaxies. Similar to the [N II]/[S II] ratio shown in Figure 10(a), the metallicity in local star-forming galaxies begins to flatten at low masses ($M_* \lesssim 10^{9.2}\,M_\odot$) (see Section 3.5). Except for the low-metallicity tail, the average points of local galaxies and those of the FMOS sample are well fit with the model of Zahid et al. (2014a, see Section 5.3). The MZ relation for the FMOS sample is qualitatively equivalent to the results based on the [N II]/Hα ratios (shown in Figure 14(b)), thus indicating that the metallicities of high-z galaxies are, on average, smaller than those in local galaxies at low masses, and that they increase with stellar mass, reaching a level similar to local galaxies at $M_* \gtrsim 10^{11}\,M_\odot$. However, we note that the metallicity range spanned by our sample ($8 \lesssim 12 + \log(\mathrm{O/H}) \lesssim 8.9$) is slightly different from that of the $N2$-based metallicity with the calibration of Maiolino et al. (2008) ($8.4 \lesssim 12 + \log(\mathrm{O/H}) \lesssim 9.1$). We remind readers that there are likely systematic uncertainties in the absolute metallicity calibrations based on different techniques and/or indicators (e.g., Kewley & Ellison 2008). It is worth noting that the $N2$-based MZ relation at $z \sim 1.6$ shows a slightly larger offset from the local relation (Figure 14(b)) than that based on the calibration of Dopita et al. (2016). Comparing the deviations of the high-z sample to the scatter of the local MZ relation (dashed lines in Figures 14(b) and 15), we find that the $N2$-based metallicity of the FMOS galaxies is offset from the local average by about five times the local scatter in the lowest mass bin, while the deviation is about three times the scatter based on the other indicator. This is most likely explained by the different sensitivities of these metallicity indicators to the ionization parameter as described above and in Section 5.1.

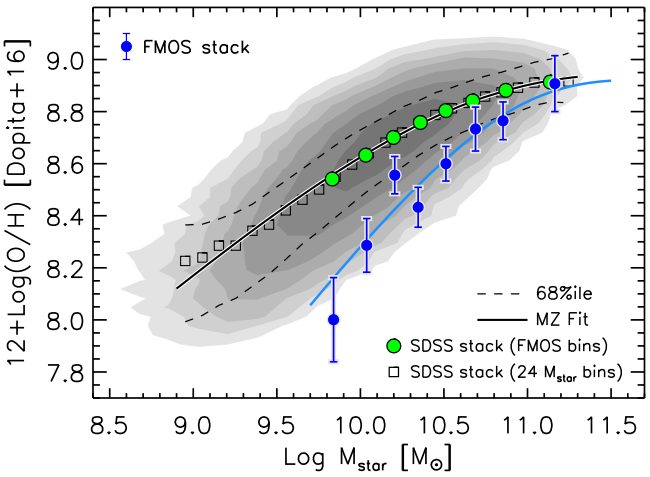

Figure 15. Mass–metallicity relation based on a calibration introduced by Dopita et al. (2016, Equation (8)). Symbols are the same as those in Figure 14. Solid curves show the best-fit relation parameterized in Equation (9) for the FMOS (blue) and the local (black) samples.

In this analysis, we remove galaxies with $N2 > -0.1$ so as to exclude AGNs (see Section 2.6). However, there is still a possibility that the average [N II]/Hα ratios are enhanced by weak AGNs. Therefore, we examine whether the metallicity measurements are affected by the changes in selecting which galaxies to stack. We lower the threshold to $N2 = -0.3$, thus excluding all galaxies with values above this limit. We find that galaxies at the high-mass end still have metallicities in agreement with local massive galaxies. Therefore, we conclude that the most massive galaxies are fully mature, as reported when using the $N2$-based metallicity.

5.3. Evolution of the Mass–Metallicity Relation

Zahid et al. (2014a) introduced the concept of a universal relation between metallicity and the stellar-to-gas mass ratio, $M_*/M_{\rm gas}$, as the underlying origin of the MZ relation. In this framework, an observed MZ relation can be parameterized as

$$12 + \log(\mathrm{O/H}) = Z_0 + \log\left[1 - \exp\left(-\left[\frac{M_*}{M_0}\right]^{\gamma}\right)\right]. \quad (9)$$

Here, Z_0 is the asymptotic metallicity at the massive end, M_0 is the characteristic stellar mass where the relation begins to flatten, and γ is the power-law slope of the relation at $M_* \ll M_0$. Given the assumption of a power-law relation between stellar and gas mass, $M_{\rm gas} \propto M_*^{\delta}$ (Peeples et al. 2014), the term $(M_*/M_0)^{\gamma}$ approximately equals $M_*/M_{\rm gas}$, and the slope γ is prescribed by the slope δ as $\gamma = 1 - \delta$ (Zahid et al. 2014a).

We model the observed MZ relations based on both the two metallicity indicators described in Sections 5.1 and 5.2 with Equation (9). This fitting function differs from the function used in our previous study (Zahid et al. 2014b) and has a more physically motivated form. We note that fitting the current measurements with the model given in Zahid et al. (2014b) yields results consistent with those found in our past study. The best-fit parameters in Equation (9) are listed in Table 3. For our sample, the stacked measurements in eight stellar mass bins are used for the fit. To derive the local MZ relation, we fit the same

Table 3
Best-fit Parameters of the Mass–Metallicity Relation[a]

Sample	Redshift[b]	Z_0	$\log(M_0/M_\odot)$	γ
Indicator: [N II]/Hα (Maiolino et al. 2008), Equation (7)				
SDSS	0.07	9.086 ± 0.003	9.87 ± 0.02	0.56 ± 0.01
FMOS	1.55	9.07 ± 0.15	10.50 ± 0.34	0.71 ± 0.45
FMOS	1.55	[9.086][c]	10.59 ± 0.05	[0.56]
Indicator: Dopita et al. (2016), Equation (8)				
SDSS	0.07	8.95 ± 0.01	10.35 ± 0.05	0.55 ± 0.01
FMOS	1.55	8.92 ± 0.22	10.71 ± 0.49	0.83 ± 0.30
FMOS	1.55	[8.95]	10.94 ± 0.08	[0.55]

Notes.
[a] The MZ relation is parameterized in Equation (9).
[b] Median redshift of each sample.
[c] Values given in square brackets have been fixed to the SDSS values.

formulation to the median values in 24 stellar mass bins at $10^{8.9} \leqslant M_*/M_\odot \leqslant 10^{11.3}$.

In Figure 14(b), the model represents well the observed *N*2-based MZ relations at $z \sim 0$ and $z \sim 1.6$. Z_0 and γ are statistically consistent between the two samples. Therefore, the evolution of the MZ relation can be quantified by the evolution of the turnover mass M_0. Motivated by this fact, we fit a model to our data with Z_0 and γ fixed to the local values ($Z_0 = 9.086$ and $\gamma = 0.56$; see Table 3). In this case, we find M_0 to be consistent with the case where Z_0 and γ are free parameters. Therefore, the evolution of the MZ relation from $z \sim 1.6$ to the present day is characterized by the decline in the turnover stellar mass M_0 by about 0.6 dex. Likewise, the model also fits well the local and high-z MZ relations based on the metallicity indicator of Dopita et al. (2016) as shown in Figure 15. However, the best-fit values of M_0 for low-z or high-z samples are slightly different from those of the *N*2-based MZ relation and show less evolution in M_0 ($\Delta \log M_0 = 0.36$ dex) for the metallicity indicator of Dopita et al. (2016).

Figure 16 shows the metallicity (from the [N II]/Hα ratio) as a function of $\gamma \log(M_*/M_0)$ for the local sample and the FMOS sample (free Z_0, γ—filled circles; fixed Z_0, γ—open circles). The measurements from our FMOS sample agree well with the local relation. In the context of the model given in Equation (9), we have $(M_*/M_0)^\gamma \sim M_*/M_{\rm gas}$ (see Zahid et al. 2014a for details), thus our results support the existence of a universal relation between the metallicity and the stellar-to-gas mass ratio from $z \sim 1.6$ to the present day. The decline of M_0 with cosmic time is simply interpreted as a result of gas consumption and stellar mass assembly through star formation. We also note that our results are consistent with a time-invariant slope of the M_*–$M_{\rm gas}$ relation, while the errors on γ are too large to constrain its evolution (if any).

However, selection effects may be present at low masses that impact our determination of γ. Our sample is potentially biased toward a population having high SFRs and being less obscured by dust (see Section 2.7). This bias may be induced by the observational limit of detecting Hα and the self-imposed selection on the predicted Hα flux. The amount of metals is commonly known to be correlated with the amount of dust (e.g., Issa et al. 1990; Schmidt & Boller 1993; Lisenfeld & Ferrara 1998). Therefore, such a bias may impact the shape of the MZ relation. In particular, the effects may be considerable at low masses because low-mass dusty galaxies, which are expected to have a low Hα flux and to be more metal-rich,

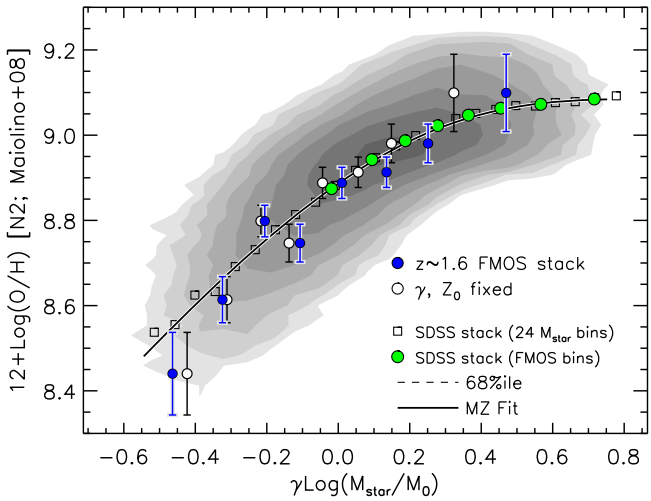

Figure 16. Metallicity vs. $\gamma \log(M_*/M_0)$, a proxy for the stellar-to-gas mass ratio (see Section 5.3), for the local and FMOS samples. Blue circles show the FMOS stacked measurements for the best-fit Z_0 and γ, while circles are for Z_0 and γ fixed to the local values. Contours and symbols representing the local sample are the same as in Figure 14(b). A solid curve is given by Equation (9) with the best-fit parameters for the local sample. Dashed lines indicate the 68th percentiles. Excellent agreement between the two samples at $z \sim 0$ and $z \sim 1.6$ suggests the existence of a universal relation between metallicity and stellar-to-gas mass ratio.

could fall below our selection limit. In addition, as naturally expected from the fact that high-z galaxies have a higher ionization parameter, galaxies with higher sSFR may have a higher ionization parameter than counterparts with lower sSFR at fixed M_*, although our data do not show any evidence for the positive correlation between these quantities. If this is the case, the cut on predicted Hα flux or the S/N makes the selected sample biased toward having higher ionization parameters, thus resulting in lower [N II]/Hα ratios (see Section 5.1). As a consequence of these possible biases, the measurements at the low-mass end could be biased toward lower metallicities, leading to an MZ relation with a steeper slope. Indeed, such biases arise in the local relation as well, where a high S/N or luminosity threshold of the Hα line is applied. A selection of local galaxies with an observed $L(\mathrm{H}\alpha) \geqslant 10^{41}$ erg s^{-1} yields a slightly steeper slope $\gamma = 0.61 \pm 0.03$ for the *N*2-based MZ relation. In contrast, we find that the slope of the local MZ relation based on the indicator of Dopita et al. (2016) is almost insensitive to such a luminosity threshold.

In Figure 14(b), we compare our result to MZ relations derived at higher redshifts ($z \gtrsim 2$, Erb et al. 2006; Steidel et al. 2014). These MZ relations show lower metallicities than our $z \sim 1.6$ relation, while the difference is not significant at the lowest mass ($M_* \sim 10^{9.8} M_\odot$). The slope of the MZ relation of Steidel et al. is found to be approximately $\gamma = 0.34$, which is shallower than found in the local MZ relation, and no flattening feature appears over the proved stellar mass range. In contrast, Wuyts et al. (2014) report that the shape of the MZ relation does not change and the turnover mass M_0 keeps increasing up to $z \sim 2.3$, by applying the same formalism (Equation (9)) to a compilation of samples. Beyond $z \sim 2$, the shape of the MZ relation is still poorly constrained (see also Sanders et al. 2015). As mentioned above, selection effects probably influence the shape of the MZ relation. In particular, there is the possibility that the $z \gtrsim 2$ samples that are shown in Figure 14 miss some of the dusty galaxies, which tend to be metal-rich, because of

their UV-based selection (Erb et al. 2006; Steidel et al. 2014). Furthermore, effects from changes in the ionization parameter and/or the ionizing radiation field are likely to be considerable at higher redshift (Steidel et al. 2016).

6. MASS–METALLICITY–SFR RELATION

Observations of an anticorrelation between metallicity and SFR at fixed stellar mass have advocated a simple picture, in which upward fluctuations in the inflow of metal-poor gas fuel star formation, while diluting the gas-phase metal abundance (e.g., Ellison et al. 2008; Mannucci et al. 2010). Mannucci et al. (2010) proposed the so-called fundamental metallicity relation, a universal relation between stellar mass, metallicity, and SFR, holding for star-forming galaxies both locally and up to $z \sim 2.5$. However, the actual shape of the FMR is known to depend on the methodology with which the three parameters are measured (see, e.g., Andrews & Martini 2013; Kashino et al. 2016). While the anticorrelation between SFR and Z appears to be characteristic of local low-mass galaxies ($M_* \lesssim 10^{10}\,M_\odot$; see, e.g., Yates et al. 2012), it remains to be demonstrated conclusively whether such a relation exists at $z > 1$ and whether the FMR is truly fundamental (i.e., does not evolve with redshift).

6.1. Anticorrelation between Metallicity and SFR

Most recent studies at $z \sim 2$ find no significant (anti) correlation between metallicity and SFR at fixed stellar mass (Steidel et al. 2014; Wuyts et al. 2014; Sanders et al. 2015). In contrast, we previously reported on a Z–SFR anticorrelation by using an sBzK-selected subset of the current data (Zahid et al. 2014b). Salim et al. (2015) also find a weak anticorrelation at $z \sim 2$ based on individual measurements, as do Guo et al. (2016) at $z \sim 0.6$. Salim et al. (2015) argue that binning by SFR (or sSFR) washes out a weak SFR dependence of metallicity when using data of low S/N. With the current data, we examine again whether metallicity depends on SFR at given stellar mass. Here, we use the [N II]/Hα ratios to determine metallicity since the indicator of Dopita et al. (2016) is known to be less sensitive to instantaneous fluctuations of the metallicity due to infalling gas (Kashino et al. 2016).

To investigate the relation between SFR and Z at fixed M_*, we derive the excess both in $\log([\mathrm{N\,II}]/\mathrm{H}\alpha)$ and in SFR for individual FMOS galaxies. The $N2$ excess is defined as the deviation from the average M_*–$N2$ relation that is converted from the best-fit MZ relation as shown in Figure 14(b). Similarly, the Hα-based SFR excess, $\mathrm{SFR}/\langle\mathrm{SFR}\rangle_{\mathrm{MS}}$, is defined as the distance from the star-forming main sequence (see Figure 1). We note that our conclusions do not change if the absolute values of sSFR or $\log([\mathrm{N\,II}]/\mathrm{H}\alpha)$ are used instead of these quantities normalized by the corresponding average values.

In Figure 17, we present the $N2$ excess as a function of the SFR excess in four stellar mass bins. We find a moderate anticorrelation between SFR and Z at all masses for the individual FMOS galaxies with a [N II]/Hα measurement. From the lowest to the highest mass bins, the Spearman's rank correlation coefficients and the confidence levels are respectively $\rho = -0.32$ (>99%), -0.28 (>99%), -0.22 (98%), -0.11 (75%). However, the individual points preferentially fall above $\Delta\log([\mathrm{N\,II}]/\mathrm{H}\alpha) = 0$ (dotted lines in Figure 17). This clearly indicates that the bias concerning the detection of the faint [N II] line certainly exists in the individual measurements. In particular, the [N II] line for low-Z galaxies tends to be much fainter than Hα and can only be detected when their SFRs are high. Therefore, [a Z–SFR] anticorrelation found with these individual measurements is likely caused by such a bias. In fact, stacked measurements, based on two subsamples binned by SFR excess in each mass bin, fall below the individual points and do not show any significant dependence of Z on SFR. While this contradiction is possibly due to the effects of sample selection, it is still desirable to further study this issue with a larger sample and accurate SFR estimation to constrain a correlation (possibly weak if any) between metallicity and SFR.

6.2. Comparison with the Local FMR

We examine the cosmic evolution of the relation between metallicity, stellar mass, and SFR. It is worth noting that a lack of a significant Z–SFR correlation at a given single redshift (i.e., within a narrow sSFR range) does not mean that this correlation is lacking over a wider sSFR range with consideration of the redshift evolution of the main sequence. In the context of the FMR, the redshift evolution of the MZ relation is expressed as a shift on the surface of the M^*–Z–SFR space while these quantities vary with cosmic time. Mannucci et al. (2010) defined a quantity combining M_* and SFR as $\mu = \log M_* - \alpha \log \mathrm{SFR}$, where the projection parameter α is determined to minimize the dispersion in metallicity over small intervals on a grid of the M_*–SFR plane. We choose $\alpha = 0.32$ for comparison with the original FMR by Mannucci et al. (2010), although $\alpha = 0.30$ is derived for the [N II]/Hα-based metallicity by Andrews & Martini (2013) and Zahid et al. (2014b). The use of $\alpha = 0.30$ does not change our conclusions. We note that Mannucci et al. (2010) use the metallicity calibration of Maiolino et al. (2008), the same as implemented here.

Figure 18 shows the metallicity derived from the [N II]/Hα ratio as a function of the projected axis, μ, with the FMR from Mannucci et al. (2010). The line ratios are measured on the composite spectra of Sample-1 in eight bins of either the μ value or stellar mass. In the latter case, the values of μ are calculated from the median stellar mass and SFR in each bin. Here, we show the results obtained using Hα-based SFRs; our conclusion does not change when using SED-based SFRs. The measurements of two binned cases (μ-bin or M_*-bin) are consistent within the uncertainties. Our FMOS sample shows good agreement with the FMR of Mannucci et al. (thin solid curve in Figure 18) at $\mu \sim 9.5$, while there is an offset toward higher metallicities at $\mu \gtrsim 10$. However, we note that Mannucci et al. (2010) derived the FMR using *in-fiber* SFRs, which are not corrected for light loss outside the fiber aperture, while we derive the *total* SFRs for our FMOS sample, accounting for the fiber loss. The use of a mixture of total and in-fiber SFRs may be misleading and result in an inaccurate physical understanding. Therefore, we derive a new relation between μ and metallicity for local galaxies, using total SFRs, for which the aperture effect and dust extinction are taken into account (see Section 2.9), as done in Zahid et al. (2014b). We note that the metallicity is based on in-fiber emission-line fluxes, and thus is not a galaxy-wide value, which possibly causes a bias toward higher O/H. To minimize the effect of such a bias, we select local galaxies with $z \geqslant 0.04$ following Kewley et al. (2005). Our high-redshift measurements are in good agreement at $\mu > 9.8$ with the local measurements, based on the median [N II]/Hα ratios in 24 bins of μ. In contrast,

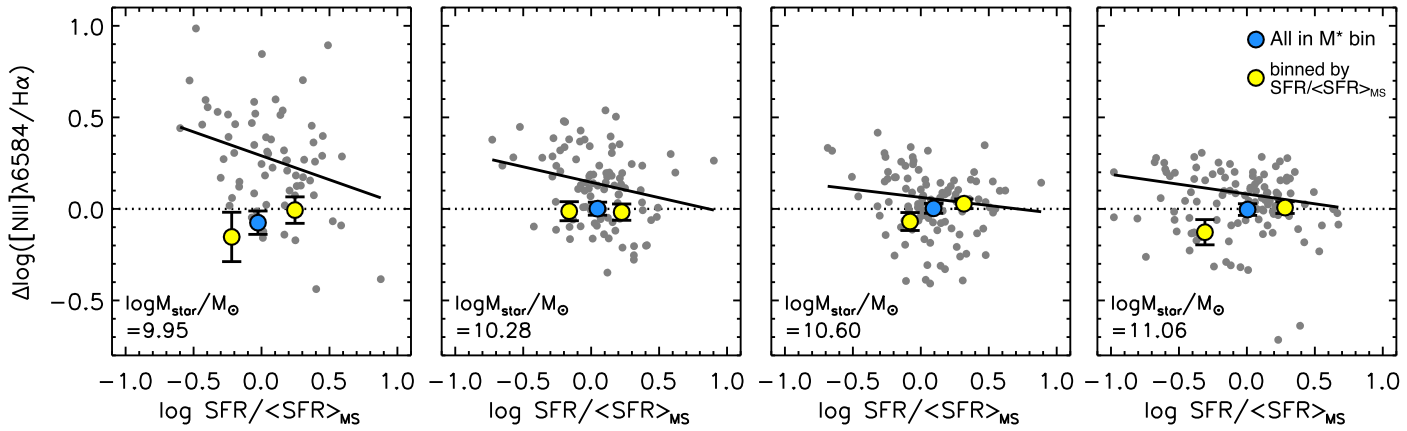

Figure 17. Excess in the [N II]/Hα ratio vs. the SFR excess in four bins of stellar mass (median M_* is shown in each panel). Individual FMOS galaxies with a [N II]/Hα measurement are shown as gray circles. In each bin, a solid line is a linear fit to individual points. Stacked points of all galaxies in each M_* bin and two subsets further separated by the SFR excess are shown by blue and yellow circles, respectively. The individual points show a moderate anticorrelation between the two quantities in all bins, while the stacks do not.

there is a difference between the local and high-z samples at $\mu < 9.8$. At the low-mass end, the offset is approximately $\Delta \log(\mathrm{O/H}) \sim 0.2$ dex in the FMR and about 0.4 dex in the MZ relation (Figure 14(b)). Here, we highlight that there still remains a significant offset in the metallicity between the relations at these two epochs in spite of the fact that the potential bias toward high SFRs in our sample is mitigated by computing the projection axis μ. In conclusion, our data do not support an extrapolation of the FMR from local galaxies to $z \sim 1.6$, as first reported in Zahid et al. (2014b), particularly at low M_* and high SFR.

6.3. Mass–Z–SFR Relation with a Gas Regulation Model

Maier et al. (2014) have studied the FMR at $z > 2$ and found that high-z galaxies in their sample are consistent with a universal FMR that is based on the physically motivated formulation by Lilly et al. (2013) (see also Onodera et al. 2016), but not with the FMR of Mannucci et al. In the framework of Lilly et al. (2013), the equilibrium gas-phase metallicity, $Z_{\rm eq}$, is determined by the regulation of star formation by the mass of gas in a galaxy, and is given as a function of M_* and SFR. We follow the parameterization of Equation (3) in Maier et al. (2014):

$$Z_{\rm eq} = Z_{\rm in} + \frac{y}{1 + \lambda(1-R)^{-1} + \varepsilon^{-1}((1+\beta-b)\mathrm{SFR}/M_* - 0.15)} \quad (10)$$

where $Z_{\rm in}$ is the metallicity of the infalling gas, y is the yield, $R = 0.27$ (for a Salpeter IMF) is the fraction of mass returned to the ISM, $\lambda \propto M_*^a$ is the mass-loading factor, and $\varepsilon = \mathrm{SFR}/M_{\rm gas} \propto M_*^b$ is the SFE. $\beta = -0.25$ is the slope of the relation between stellar mass and sSFR, i.e., $\mathrm{sSFR} \propto M_*^\beta$. Although Lilly et al. (2013) assume $R = 0.4$ and $\beta = -0.1$, the use of such different values does not change our conclusions. We note that Equation (10) is a form for $z = 0$ and that the form for high redshifts will depend on the time variation of parameters, as discussed in Lilly et al. (2013). In particular, the SFE is likely to increase with redshift (e.g., Genzel et al. 2015). Here, we compare our measurements at $z \sim 1.6$ to this model without considering the time dependence of the parameters to examine whether our FMOS galaxies at $z \sim 1.6$ follow a nonevolving M_*–Z–SFR relation.

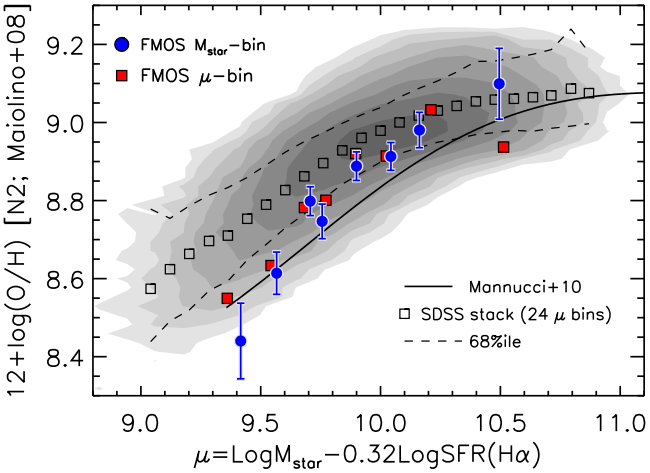

Figure 18. Projected M_*–Z–SFR relation: metallicity vs. $\mu_{\alpha=0.32}(M_*, \mathrm{SFR})$. Metallicities are based on [N II]/Hα and μ is calculated using Hα-based SFRs for both the local and FMOS samples. Symbols indicate the stacked points in eight bins of M_* (blue circles) or μ (red squares). Shaded contours show local star-forming galaxies, with the stacked data points in 24 equally spaced bins of μ (squares) and the central 68th percentiles (dotted lines). A thin solid line indicates the original FMR derived by Mannucci et al. (2010) (based on in-fiber SFRs).

We determine the parameters from a model fitting for the local sample using total SFRs, as listed in Table 4. We use SDSS galaxies with $9.2 \leqslant \log M_*/M_\odot \leqslant 10.6$ and $-1 \leqslant \log \mathrm{SFR}/(M_\odot\ \mathrm{yr}^{-1}) \leqslant 1$, which are binned by $\Delta \log M_* = 0.1$ dex and $\Delta \log \mathrm{SFR} = 0.1$ dex. We utilize the MPFIT2DFUN IDL procedure (Markwardt 2009) to fit the model to the median metallicity in each bin as a function of both M_* and SFR. $Z_{\rm in}$ is fixed to zero while the use of a different value in the range $0 < Z_{\rm in}/y < 0.1$ does not change our conclusions, although the best-fit values of other parameters will change slightly. The derived values are nearly equivalent to those given in Lilly et al. (2013).

Based on this gas regulation model, we find that our FMOS sample at $z \sim 1.6$ is consistent with a nonevolving FMR relation. Figure 19 shows average metallicities for galaxies in our sample and for local objects, as a function of (a) SFR and (b) sSFR for

Table 4
Fit of the FMR model of Lilly et al. (2013) to the SDSS sample

$\log y$	λ_{10}	a	ε_{10}^{-1} (Gyr)	b
9.09 ± 0.01	0.38 ± 0.05	-0.61 ± 0.03	1.9 ± 0.3	0.48 ± 0.05

Note. Parameters in Equation (10): y—yield parameter given in units of $12 + \log(\mathrm{O/H})$; λ_{10}—mass-loading factor at $M_* = 10^{10}\,M_\odot$, ε_{10}—star formation efficiency at $M_* = 10^{10}\,M_\odot$.

galaxies of different stellar masses, in comparison with the best-fit $Z(M_*, \mathrm{SFR})$ relation. We first separate the local sources into mass bins 0.2 dex wide, and divide each mass bin into 40 SFR bins. The median metallicities are shown separately for each mass bin, as color-coded in the plot. The functional form of $Z(M_*, \mathrm{SFR})$ (Equation (10)) reproduces the behavior of local galaxies in each mass bin (dashed curves). The FMOS stacked data points are based on the co-added spectra of Sample-1 in eight mass bins. Figure 19 shows good agreement between our $z \sim 1.6$ measurements and the model prediction extrapolated from the local sample within $\Delta \log(\mathrm{O/H}) \sim 0.1$ dex at each M_*. This is more clearly seen in the lower panels (d) and (e), in which we show the deviations of observed metallicities from the model values at corresponding M_* and SFR.

The agreement between our data and the model is also seen in panels (c) and (f) of Figure 19, where we present the MZ relation and the deviation in metallicity from the model for the local galaxies (squares) and FMOS galaxies (filled circles), respectively. We separate the local sample into SFR bins 0.3 dex wide, then divide each into 40 M_* bins. The median metallicities are presented as a function of M_* separately for each SFR bin as color-coded. We overlaid the predictions from the best-fit FMR at the median SFR of each bin for the local sample (dashed lines) and our FMOS sample (solid lines), and mark the expected metallicities at the median M_* and SFR of each bin of the FMOS sample (open diamonds), which are in good agreement with the data points.

Our measurements at low masses require a rapid decline of metallicity at higher SFRs (see Figures 19(a) and (b)). This trend is naturally induced by considering the evolution of galaxies as regulated by the gas content, taking account of gas inflow and mass loss in the model of Lilly et al. (2013). Our finding is consistent with the conclusion in Maier et al. (2014), claiming that whether an FMR is truly fundamental (i.e., independent of redshift) depends on the formulation of the model and its extrapolation to regions of the M_*–SFR parameter space different from that occupied by local galaxies. Lastly, we note that, in this study, we do not take the time evolution of model parameters into account.

7. CONCLUSIONS

We investigate the physical conditions of the ionized gas in star-forming galaxies on the main sequence at $1.43 < z < 1.74$ using a sample of 701 galaxies with an Hα detection from the FMOS-COSMOS survey. This is the first time that such a large sample over a wide stellar mass range of $10^{9.6} \lesssim M_*/M_\odot \lesssim 10^{11.6}$ has been used at these redshifts. Based on the X-ray imaging data set from the *Chandra*-COSMOS Legacy survey, we carefully exclude the AGN contamination and make sure that ionization due to AGNs does not impact our stacked measurements of the emission-line ratios. Our main results are as follows:

1. We confirm a clear offset of star-forming galaxies at $z \sim 1.6$ from the sequence of local star-forming galaxies in the BPT diagram using both individual and stacked measurements (Figures 4 and 5). This offset amounts to an increase in the [O III]/Hβ ratio by a factor of $\sim$3 in the mass–excitation diagram (M_* versus [O III]/Hβ; Figure 6) between our FMOS sample and local SDSS galaxies.
2. We measure the emission-line ratio [S II] $\lambda\lambda$6717, 6731/Hα with co-added spectra and find lower values of [S II]/Hα for the highest two mass bins ($M_* \gtrsim 10^{10.6}\,M_\odot$) as compared with local star-forming galaxies at fixed [O III]/Hβ (Figure 7). These lower [S II]/Hα ratios are an indication of a higher ionization parameter of the ISM than of local galaxies.
3. The average electron density is measured based on the emission-line ratio [S II] λ6717/[S II] λ6731 using stacked spectra and gives a value of $n_\mathrm{e} = 222^{+172}_{-128}\ \mathrm{cm}^{-3}$, which is higher than the average value in local star-forming galaxies ($n_\mathrm{e} \sim 10$–$10^2\ \mathrm{cm}^{-3}$; Figure 9).
4. Comparisons with theoretical models indicate a relatively high ionization parameter ($\log q_\mathrm{ion}/c \sim -3$) for H II regions in galaxies at $z \sim 1.6$, which is approximately 0.3 dex higher than for local star-forming galaxies at a fixed stellar mass (Figure 11). Given our measurement of a relatively high gas density, a higher ionization parameter could reflect an increase in the efficiency of star formation expected for high-z galaxies.
5. We find that the enhancement in the ionization parameter *at fixed metallicity*, i.e., a higher q_ion than expected from the local q_ion–Z anticorrelation, is essential to produce the offset of high-z galaxies with $M_* \gtrsim 10^{10}\,M_\odot$ from the loci of local galaxies in the emission-line diagrams. Furthermore, additional effects, attributed to a higher electron density and a hardening of the ionizing radiation field, are likely important as well (Figure 12). In contrast, the changes in emission-line ratios in lower-mass, $z \sim 1.6$ galaxies ($M_* < 10^{10}\,M_\odot$) could be explained by just the increase in q_ion accompanying the change in metallicity without invoking additional effects.
6. We derive the mass–metallicity relation from the [N II]/Hα ratio for our $z \sim 1.6$ sample (Figure 14). Our results are consistent with the previous derivation for an sBzK-selected subsample in the FMOS-COSMOS survey (Zahid et al. 2014b). The current data strengthen our previous result: the most massive galaxies ($M_* \gtrsim 10^{11}\,M_\odot$) are fully mature at a level similar to local galaxies, while, at the lowest masses ($M_* \sim 10^{9.8}\,M_\odot$), the metallicity is on average $\sim$0.4 dex smaller than in local galaxies. Our sample at $z \sim 1.6$ is in good agreement with a universal metallicity relation proposed by Zahid et al. (2014a), which is founded on the fundamental relation between metallicity and stellar-to-gas mass ratio. However, we highlight that the recipes for determining metallicity at high redshift may need further refinement due to changes in ionization parameter, hardness of stellar spectra, and the N/O versus O/H relation (if any).
7. We evaluate metallicity adopting a new calibration by Dopita et al. (2016), which uses the line ratios [N II]/[S II] and [N II]/Hα (Figure 15) and assumes universality of the local N/O versus O/H relation. The novelty of this indicator is that it is less sensitive to changes in the ionization parameter. The derived mass–metallicity relation

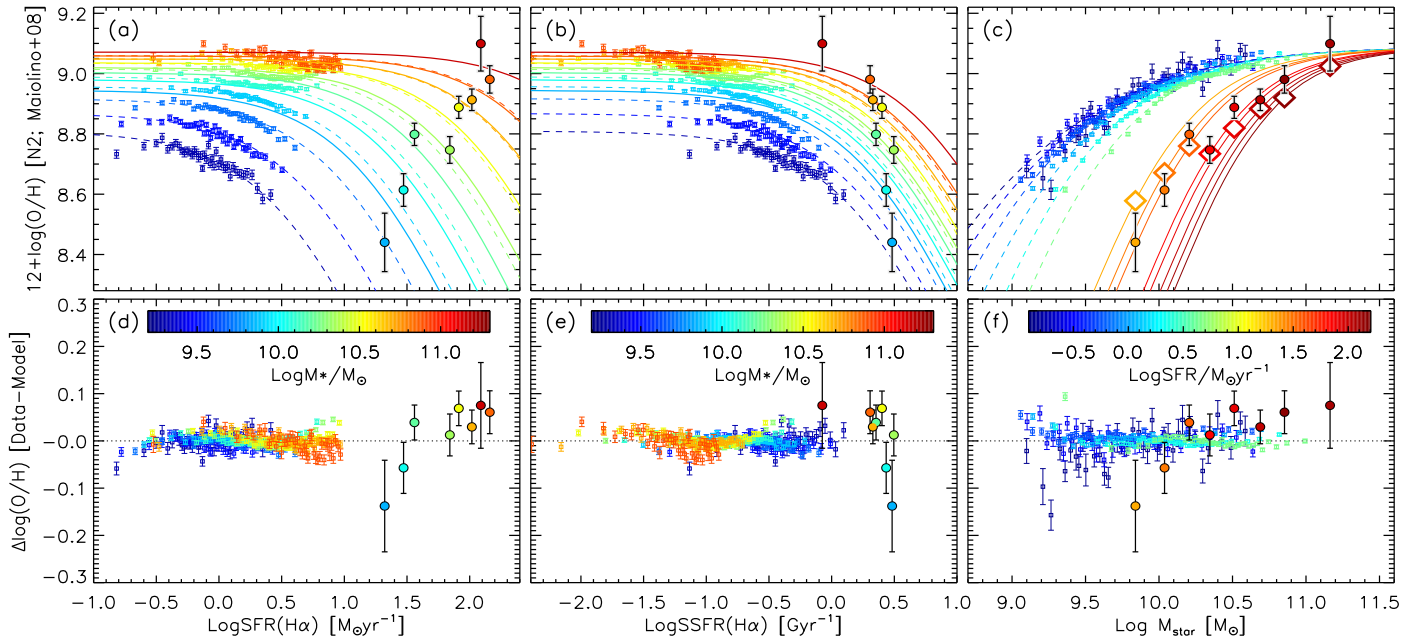

Figure 19. Metallicity as a function of (a) SFR, (b) sSFR, and (c) stellar mass, as compared to the model of Lilly et al. (2013). The FMOS measurements (Sample-1) based on composite spectra in eight mass bins are indicated by filled circles, color-coded by M_* (panels (a) and (b)) or SFR (panel (c)). Colored squares show median metallicities of local galaxies in bins of stellar mass and SFR. Dashed lines show the model metallicity, $Z(M_*, \mathrm{SFR})$, at median M_* (panels (a) and (b)) or SFR (panel (c)). Solid lines indicate the model metallicities for median M_* or SFR of our FMOS sample. In panel (c), diamonds indicate the metallicities predicted by the best-fit $Z(M_*, \mathrm{SFR})$ at the median M_* and SFR of each bin of our FMOS sample. (d)–(f) Differences between observed metallicities and theoretical predictions from the model fit (related to panels (a), (b), and (c), respectively).

shows a trend that is qualitatively equivalent to that seen in the relation based on the [N II]/Hα ratio, while the absolute value of the metallicity is slightly different. In addition, the MZ relations based on this new indicator show an offset, between the SDSS and FMOS samples, that is three times as large as the scatter of the local MZ relation at $M_* \sim 10^{9.8}\,M_\odot$, while the [N II]/H$\alpha$-based MZ relations show an offset five times the local scatter. This difference between the two metallicity indicators may be caused by the fact that the indicator of Dopita et al. (2016) is relatively insensitive to variations in the ionization parameter.

8. The evolution of the MZ relation from $z \sim 1.6$ to the present day is well characterized by the change in the turnover stellar mass at which the metallicity begins to saturate. As a consequence, the MZ relations at both epochs are described by a universal relation between metallicity and the stellar mass normalized by the turnover mass, which is a proxy for the stellar-to-gas mass ratio in the context of a simple chemical evolution model (Figure 16).
9. We revise the FMR proposed by Mannucci et al. (2010) by using the total SFRs instead of in-fiber SFRs (as done in Zahid et al. 2014b) and find that our FMOS sample shows lower metallicities than expected for their M_* and SFR from the extrapolation of the FMR (Figure 18). In contrast, our data are consistent with a physically motivated model from Lilly et al. (2013), in which the star formation is instantaneously regulated by the gas mass, gas inflow, and mass loss by outflows. This model well reproduces a rapid decline in metallicity at high SFRs as shown in our data (Figure 19).

To conclude, our study has established the rest-frame optical emission-line properties of star-forming galaxies at $z \sim 1.6$ and identified the processes likely responsible for differences from local samples such as shown with the BPT diagram. The FMOS-COSMOS project and other related efforts have enabled us to take an important step forward in understanding the evolution of the ISM in galaxies at the peak epoch of the cosmic star formation history, which will be carried forward by the next generation of multi-object spectrographs (e.g., Subaru/PFS, VLT/MOONS).

We are grateful to the referee for careful reading and useful comments, M. Dopita for kindly providing us with the photoionization model data, and M. Fukugita, K. Yabe, T. Kojima, and R. Shimakawa for useful discussions. We thank the Subaru telescope staff, especially K. Aoki, for their great help in the observations. This paper is based on data collected at the Subaru Telescope, which is operated by the National Astronomical Observatory of Japan. We appreciate the MPA/JHU team for making their catalog public. Funding for SDSS-III has been provided by the Alfred P. Sloan Foundation, the Participating Institutions, the National Science Foundation, and the U.S. Department of Energy Office of Science. The SDSS-III web site is http://www.sdss3.org/. T.M. is supported by CONACyT Grants 179662, 252531 and UNAM-DGAPA PAPIIT IN104216. A.R. is grateful to the National Astronomical Observatory of Japan for its support and hospitality while this paper was prepared. Partial support by the INAF-PRIN 2012 grant is also acknowledged. This work was supported in part by KAKENHI (YT: 23244031 and 16H02166) through Japan Society for the Promotion of Science (JSPS). J.D.S. is supported by JSPS KAKENHI grant Number 26400221 and the World Premier International Research Center Initiative (WPI), MEXT, Japan. D.K. is supported through the Grant-in-Aid for JSPS Research Fellows (No. 26-3216).

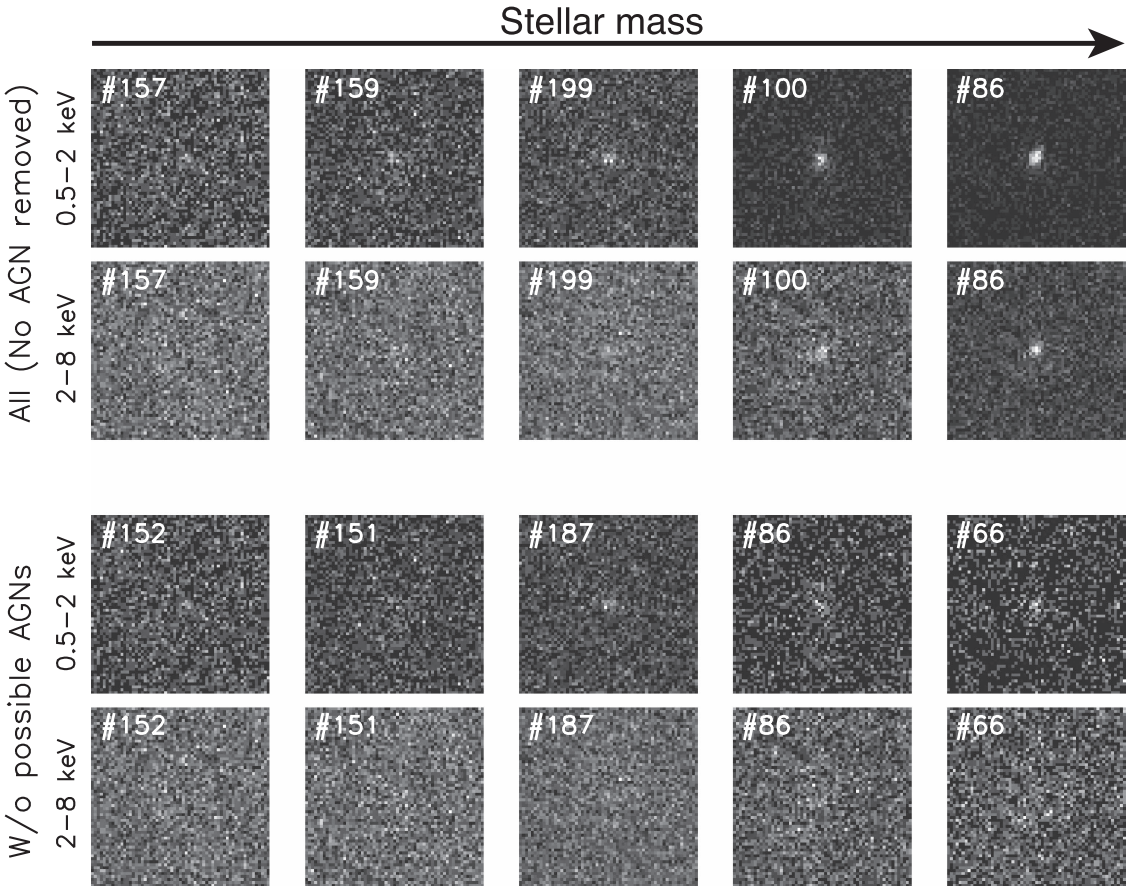

Figure 20. *Chandra* stacked X-ray images (30 arcsec on each side) in two bandpasses (soft: 0.5–2 keV, hard: 2–8 keV) of our sample in five bins of stellar mass. The number of individual images for stacking is indicated in each panel. The upper group shows the stacked images for the sample including all SED-selected galaxies without any removal of possible AGNs (case 1). The lower group shows images for the sample in which all AGN candidates are removed (case 3) for the same stellar mass ranges as above. The stellar mass increases from left to right (see Table 5).

APPENDIX
ASSESSMENT OF AGN CONTAMINATION

As described in Section 2.6, we remove AGNs from our star-forming galaxy samples for all analyses in this paper. Our data, as presented on line-ratio diagrams (Figures 4, 7, and 8), show no strong signature of ionizing radiation from AGNs. However, the possibility that weak and/or obscured AGNs affect the results cannot be completely ruled out. Here, we assess the contribution of such hidden AGNs to the results based on the co-added spectra.

X-ray emission is an effective indicator of the existence of an AGN. We measure the average X-ray luminosities of our FMOS galaxies by stacking the *Chandra X-ray Observatory*/Advanced CCD Imaging Spectrometer (ACIS-I) images from the *Chandra*-COSMOS Legacy survey (Elvis et al. 2009; Civano et al. 2016) using the CSTACK tool[26] (v4.3; Miyaji et al. 2008). To examine how the X-ray luminosity depends on the exclusion of individually identified AGNs, we compare three samples with different criteria for the removal of possible AGNs: (1) no AGN cut is applied, (2) excluding individual X-ray-detected sources, and (3) excluding all possible AGN candidates (X-ray sources, FWHM(Hα) $>$ 1000 km s^{-1}, or identified with the BPT diagram; see Section 2.6). The last case is implemented for the results based on stacking analysis throughout the paper. Figure 20 shows the stacked X-ray images in five bins of stellar mass, separately in two bandpasses (soft: 0.5–2 keV, hard: 2–8 keV), from the two samples without (case 1) and with (case 3) AGN removal.

The average count rate is converted into flux assuming a spectrum with $\Gamma = 1.7$ and a Galactic column density $N_{\rm H} = 2.7 \times 10^{20}$ cm^{-2} (Dickey & Lockman 1990; Elvis et al. 2009). The average rest-frame X-ray luminosity is calculated from Equation (4) in Lehmer et al. (2008), with a median redshift ($z \simeq 1.6$). Table 5 lists the X-ray luminosities and associated errors in each bin. When no AGN cut is applied (case 1), the X-ray emission is significantly detected in the two most massive bins at S/N $>$ 5 in both the soft and hard bandpasses. When the AGN cut is applied (cases 2 and 3), only the most massive bin ($\log M_*/M_\odot > 11.1$) presents a significant detection (S/N $>$ 3) in the X-ray band. In the third and fourth bins ($10.4 < \log M_*/M_\odot < 11.1$), the X-ray emission is detected at a significance of S/N $\sim$ 2–3. There are cases with no detection (S/N $<$ 1) in the lowest two mass bins, for which there are at most a few objects that are individually detected in the X-ray band (see Table 5).

To further investigate the impact of AGNs, we compare the mean SFR and mean X-ray luminosity in the full *Chandra* bandpass ($L_{0.5-8\,\rm keV}$) in each bin in Figure 21. The mean SFRs are derived from dust-corrected Hα luminosity (see Section 2.7). Following Lehmer et al. (2008), we compare our data with an SFR–$L_{\rm X\text{-}ray}$ relation for star-forming galaxies derived by Persic & Rephaeli (2007) and a relation with three

[26] http://lambic.astrosen.unam.mx/cstack

Table 5
X-Ray Luminosity Measurements

Median $\log M_*/M_\odot$[a]	9.93	10.26	10.60	10.96	11.25
Range	[9.1:10.1]	[10.1:10.4]	[10.4:10.8]	[10.8:11.1]	[11.1:11.7]
Case 1: No AGN exclusion applied					
No. of images[b]	157	159	199	100	86
Soft[c]	0.11 ± 0.08	0.32 ± 0.09	0.28 ± 0.08	1.20 ± 0.13	2.46 ± 0.18
Hard[d]	<0.75[f]	0.58 ± 0.50	0.83 ± 0.44	3.26 ± 0.66	7.25 ± 0.80
Full[e]	<0.76	0.90 ± 0.51	1.11 ± 0.45	4.46 ± 0.68	9.71 ± 0.82
Case 2: X-ray-luminous objects removed					
No. of images	157	156	195	93	78
Soft	0.11 ± 0.08	0.24 ± 0.09	0.23 ± 0.08	0.42 ± 0.12	0.48 ± 0.13
Hard	<0.75	<0.76	0.74 ± 0.44	1.57 ± 0.66	3.43 ± 0.78
Full	<0.76	0.61 ± 0.513	0.97 ± 0.45	1.20 ± 0.67	3.92 ± 0.79
Case 3: All possible AGNs removed					
No. of images	152	151	187	86	66
Soft	<0.12	0.21 ± 0.09	0.20 ± 0.08	0.45 ± 0.12	0.50 ± 0.15
Hard	<0.77	<0.77	0.83 ± 0.45	1.48 ± 0.68	2.87 ± 0.84
Full	<0.78	<0.79	1.03 ± 0.46	1.93 ± 0.69	3.37 ± 0.85

Notes.
[a] Median stellar mass in each bin.
[b] Number of stacked images in each bin.
[c] Soft band (0.5–2 keV) luminosity in units of 10^{42} erg s^{-1}.
[d] Hard band (2–8 keV) luminosity in units of 10^{42} erg s^{-1}.
[e] Full band (0.5–8 keV) luminosity in units of 10^{42} erg s^{-1}.
[f] Upper limit is given as 1.5 times noise level if S/N < 1.

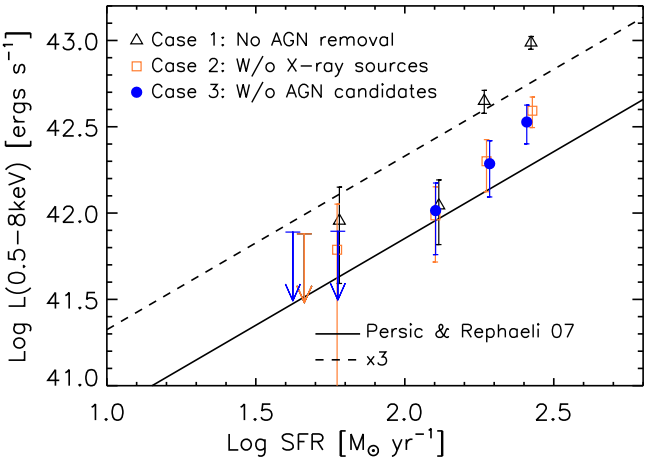

Figure 21. Comparison between the mean SFR (from dust-corrected Hα luminosity) and the 0.5–8 keV luminosity $L_{0.5-8\,\mathrm{keV}}$ in each bin of stellar mass. The X-ray luminosities $L_{0.5-8\,\mathrm{keV}}$ are measured by stacking the *Chandra* ACIS-I images. Different symbols shows the measurements for different cases of AGN removal (triangles—no AGN removed; squares—without X-ray-detected sources; filled circles—without all potential AGN candidates; see the text). An SFR–L_X relation for star-forming galaxies from Persic & Rephaeli (2007) and a relation with three times higher $L_{0.5-8\,\mathrm{keV}}$ are shown by the solid and dashed lines, respectively.

times higher X-ray luminosity, which corresponds to ∼2.5 times the rms scatter of the L_X–SFR relation, to distinguish AGNs from non-AGNs. We compare the measurements for the samples with the different X-ray exclusion criteria (cases 1–3). We see that $L_{0.5-8\,\mathrm{keV}}$ is correlated with SFR at SFR $\gtrsim 100\,M_\odot\mathrm{yr}^{-1}$ ($M_* \gtrsim 10^{10.4}M_\odot$) in all the cases and that the removal of individual X-ray-detected sources primarily affects the average X-ray luminosity of the more massive bins. As a result of the AGN exclusion, the X-ray luminosities are reduced to the level where the residual contribution from AGNs is likely to be negligible in three bins of higher stellar mass. For two lower-mass bins, upper limits on $L_{0.5-8\,\mathrm{keV}}$ are calculated as 1.5 times the noise level, as shown by downward arrows in Figure 21.

Figure 21 indicates that, once the individually detected AGNs are removed, the contribution to the X-ray luminosities in the stack from unidentified AGNs is small, and that levels of the residual X-ray luminosity are comparable to the levels that are normally expected for star-forming galaxies (solid line in Figure 21). While the limit of the lowest mass bin does not reject the probability that a contribution from AGNs exists, the AGN contribution can be expected to be negligible in such a range of stellar mass. Therefore, we conclude that the impact from AGNs in our stacking analysis is small enough to appropriately assess the properties of star-forming H II regions over the entire stellar mass range spanned by our sample.

REFERENCES

Abazajian, K. N., Adelman-McCarthy, J. K., Agüeros, M. A., et al. 2009, ApJS, 182, 543
Alam, S., Albareti, F. D., Allende Prieto, C., et al. 2015, ApJS, 219, 12
Aller, L. H. 1942, ApJ, 95, 52
Andrews, B. H., & Martini, P. 2013, ApJ, 765, 140
Arnouts, S., & Ilbert, O. 2011, LePHARE: Photometric Analysis for Redshift Estimate, Astrophysics Source Code Library, ascl:1108.009
Baldwin, J. A., Phillips, M. M., & Terlevich, R. 1981, PASP, 93, 5
Bouché, N., Hohensee, W., Vargas, R., et al. 2012, MNRAS, 426, 801
Brinchmann, J., Charlot, S., White, S. D. M., et al. 2004, MNRAS, 351, 1151
Brinchmann, J., Pettini, M., & Charlot, S. 2008, MNRAS, 385, 769
Brusa, M., Fiore, F., Santini, P., et al. 2009, A&A, 507, 1277
Bruzual, G., & Charlot, S. 2003, MNRAS, 344, 1000
Bundy, K., Georgakakis, A., Nandra, K., et al. 2008, ApJ, 681, 931
Calzetti, D., Armus, L., Bohlin, R. C., et al. 2000, ApJ, 533, 682
Chabrier, G. 2003, PASP, 115, 763
Cid Fernandes, R., Stasińska, G., Schlickmann, M. S., et al. 2010, MNRAS, 403, 1036

Civano, F., Marchesi, S., Comastri, A., et al. 2016, ApJ, 819, 62
Copetti, M. V. F., Mallmann, J. A. H., Schmidt, A. A., & Castañeda, H. O. 2000, A&A, 357, 621
Cowie, L. L., Barger, A. J., & Songaila, A. 2016, ApJ, 817, 57
Cresci, G., Mannucci, F., Maiolino, R., et al. 2010, Natur, 467, 811
Dalcanton, J. J. 2007, ApJ, 658, 941
Davé, R., Finlator, K., & Oppenheimer, B. D. 2012, MNRAS, 421, 98
Dayal, P., Ferrara, A., & Dunlop, J. S. 2013, MNRAS, 430, 2891
Dickey, J. M., & Lockman, F. J. 1990, ARA&A, 28, 215
Domgorgen, H., & Mathis, J. S. 1994, ApJ, 428, 647
Domínguez, A., Siana, B., Henry, A. L., et al. 2013, ApJ, 763, 145
Dopita, M. A., Kewley, L. J., Heisler, C. A., & Sutherland, R. S. 2000, ApJ, 542, 224
Dopita, M. A., Kewley, L. J., Sutherland, R. S., & Nicholls, D. C. 2016, Ap&SS, 361, 61
Dopita, M. A., Sutherland, R. S., Nicholls, D. C., Kewley, L. J., & Vogt, F. P. A. 2013, ApJS, 208, 10
Elbaz, D., Daddi, E., Le Borgne, D., et al. 2007, A&A, 468, 33
Ellison, S. L., Patton, D. R., Simard, L., & McConnachie, A. W. 2008, ApJL, 672, L107
Elvis, M., Civano, F., Vignali, C., et al. 2009, ApJS, 184, 158
Erb, D. 2008, in ASP Conf. Ser. 399, Panoramic Views of Galaxy Formation and Evolution, ed. T. Kodama, T. Yamada, & K. Aoki (San Francisco, CA: ASP), 239
Erb, D. K., Shapley, A. E., Pettini, M., et al. 2006, ApJ, 644, 813
Evans, I. N., & Dopita, M. A. 1985, ApJS, 58, 125
Finlator, K., & Davé, R. 2008, MNRAS, 385, 2181
Genzel, R., Tacconi, L. J., Gracia-Carpio, J., et al. 2010, MNRAS, 407, 2091
Genzel, R., Tacconi, L. J., Lutz, D., et al. 2015, ApJ, 800, 20
Groves, B., Brinchmann, J., & Walcher, C. J. 2012, MNRAS, 419, 1402
Guo, Y., Koo, D. C., Lu, Y., et al. 2016, ApJ, 822, 103
Hayashi, M., Ly, C., Shimasaku, K., et al. 2015, PASJ, 67, 80
Ilbert, O., McCracken, H. J., Le Fèvre, O., et al. 2013, A&A, 556, A55
Ilbert, O., Salvato, M., Le Floc'h, E., et al. 2010, ApJ, 709, 644
Issa, M. R., MacLaren, I., & Wolfendale, A. W. 1990, A&A, 236, 237
Iwamuro, F., Moritani, Y., Yabe, K., et al. 2012, PASJ, 64, 59
Izotov, Y. I., Stasińska, G., Meynet, G., Guseva, N. G., & Thuan, T. X. 2006, A&A, 448, 955
Juneau, S., Bournaud, F., Charlot, S., et al. 2014, ApJ, 788, 88
Juneau, S., Dickinson, M., Alexander, D. M., & Salim, S. 2011, ApJ, 736, 104
Kartaltepe, J. S., Sanders, D. B., Silverman, J. D., et al. 2015, ApJL, 806, L35
Kashino, D., Renzini, A., Silverman, J. D., & Daddi, E. 2016, ApJL, 823, L24
Kashino, D., Silverman, J. D., Rodighiero, G., et al. 2013, ApJL, 777, L8
Kauffmann, G., Heckman, T. M., Tremonti, C., et al. 2003a, MNRAS, 346, 1055
Kauffmann, G., Heckman, T. M., White, S. D. M., et al. 2003b, MNRAS, 341, 33
Kennicutt, R. C., Jr. 1998, ARA&A, 36, 189
Kewley, L. J., & Dopita, M. A. 2002, ApJS, 142, 35
Kewley, L. J., Dopita, M. A., Leitherer, C., et al. 2013a, ApJ, 774, 100
Kewley, L. J., & Ellison, S. L. 2008, ApJ, 681, 1183
Kewley, L. J., Groves, B., Kauffmann, G., & Heckman, T. 2006, MNRAS, 372, 961
Kewley, L. J., Jansen, R. A., & Geller, M. J. 2005, PASP, 117, 227
Kewley, L. J., Maier, C., Yabe, K., et al. 2013b, ApJL, 774, L10
Kewley, L. J., Zahid, H. J., Geller, M. J., et al. 2015, ApJL, 812, L20
Kimura, M., Maihara, T., Iwamuro, F., et al. 2010, PASJ, 62, 1135
Kojima, T., Ouchi, M., Nakajima, K., et al. 2016., arXiv:1605.03436
Köppen, J., & Edmunds, M. G. 1999, MNRAS, 306, 317
Koyama, Y., Kodama, T., Hayashi, M., et al. 2015, MNRAS, 453, 879
Kriek, M., Shapley, A. E., Reddy, N. A., et al. 2015, ApJS, 218, 15
Kroupa, P. 2001, MNRAS, 322, 231
Lamareille, F., Brinchmann, J., Contini, T., et al. 2009, A&A, 495, 53
Lara-López, M. A., Bongiovanni, A., Cepa, J., et al. 2010a, A&A, 519, A31
Lara-López, M. A., Cepa, J., Bongiovanni, A., et al. 2010b, A&A, 521, L53
Lara-López, M. A., Hopkins, A. M., López-Sánchez, A. R., et al. 2013, MNRAS, 434, 451
Lehmer, B. D., Brandt, W. N., Alexander, D. M., et al. 2008, ApJ, 681, 1163
Levesque, E. M., Kewley, L. J., & Larson, K. L. 2010, AJ, 139, 712
Lilly, S. J., Carollo, C. M., Pipino, A., Renzini, A., & Peng, Y. 2013, ApJ, 772, 119
Lilly, S. J., Le Fèvre, O., Renzini, A., et al. 2007, ApJS, 172, 70
Lisenfeld, U., & Ferrara, A. 1998, ApJ, 496, 145
Liu, X., Shapley, A. E., Coil, A. L., Brinchmann, J., & Ma, C.-P. 2008, ApJ, 678, 758
Madau, P., & Dickinson, M. 2014, ARA&A, 52, 415
Magdis, G. E., Daddi, E., Sargent, M., et al. 2012, ApJL, 758, L9
Maier, C., Lilly, S. J., Ziegler, B. L., et al. 2014, ApJ, 792, 3
Maier, C., Ziegler, B. L., Lilly, S. J., et al. 2015, A&A, 577, A14
Maiolino, R., Nagao, T., Grazian, A., et al. 2008, A&A, 488, 463
Mancini, C., Renzini, A., Daddi, E., et al. 2015, MNRAS, 450, 763
Mannucci, F., Cresci, G., Maiolino, R., Marconi, A., & Gnerucci, A. 2010, MNRAS, 408, 2115
Mannucci, F., Salvaterra, R., & Campisi, M. A. 2011, MNRAS, 414, 1263
Markwardt, C. B. 2009, in ASP Conf. Ser. 411, Astronomical Data Analysis Software and Systems XVIII, ed. D. A. Bohlender, D. Durand, & P. Dowler (San Francisco, CA: ASP), 251
Masters, D., Faisst, A., & Capak, P. 2016, ApJ, 828, 18
Masters, D., McCarthy, P., Siana, B., et al. 2014, ApJ, 785, 153
McCracken, H. J., Milvang-Jensen, B., Dunlop, J., et al. 2012, A&A, 544, A156
Miyaji, T., Griffiths, R. E. & C-COSMOS Team 2008, in AAS/High Energy Astrophysics Division, 10, 4.01
Nakajima, K., & Ouchi, M. 2014, MNRAS, 442, 900
Nakamura, O., Fukugita, M., Brinkmann, J., & Schneider, D. P. 2004, AJ, 127, 2511
Newman, S. F., Buschkamp, P., Genzel, R., et al. 2014, ApJ, 781, 21
Onodera, M., Carollo, C. M., Lilly, S., et al. 2016, ApJ, 822, 42
Osterbrock, D. E., & Ferland, G. J. 2006, Astrophysics of Gaseous Nebulae and Active Galactic Nuclei (Sausalito, CA: University Science Books)
Pagel, B. E. J., Edmunds, M. G., Blackwell, D. E., Chun, M. S., & Smith, G. 1979, MNRAS, 189, 95
Pagel, B. E. J., Edmunds, M. G., & Smith, G. 1980, MNRAS, 193, 219
Peeples, M. S., & Shankar, F. 2011, MNRAS, 417, 2962
Peeples, M. S., Werk, J. K., Tumlinson, J., et al. 2014, ApJ, 786, 54
Pérez-Montero, E., & Contini, T. 2009, MNRAS, 398, 949
Persic, M., & Rephaeli, Y. 2007, A&A, 463, 481
Pilyugin, L. S., Vílchez, J. M., Mattsson, L., & Thuan, T. X. 2012, MNRAS, 421, 1624
Price, S. H., Kriek, M., Brammer, G. B., et al. 2014, ApJ, 788, 86
Puglisi, A., Rodighiero, G., Franceschini, A., et al. 2016, A&A, 586, A83
Reddy, N. A., Erb, D. K., Steidel, C. C., et al. 2005, ApJ, 633, 748
Reynolds, R. J. 1984, ApJ, 282, 191
Reynolds, R. J. 1992, ApJL, 392, L35
Rudie, G. C., Steidel, C. C., Trainor, R. F., et al. 2012, ApJ, 750, 67
Sabbadin, F., Minello, S., & Bianchini, A. 1977, A&A, 60, 147
Salim, S., Lee, J. C., Davé, R., & Dickinson, M. 2015, ApJ, 808, 25
Salim, S., Rich, R. M., Charlot, S., et al. 2007, ApJS, 173, 267
Salpeter, E. E. 1955, ApJ, 121, 161
Sanders, R. L., Shapley, A. E., Kriek, M., et al. 2015, ApJ, 799, 138
Sanders, R. L., Shapley, A. E., Kriek, M., et al. 2016, ApJ, 816, 23
Schmidt, K.-H., & Boller, T. 1993, AN, 314, 361
Scoville, N., Aussel, H., Sheth, K., et al. 2014, ApJ, 783, 84
Shapley, A. E., Coil, A. L., Ma, C.-P., & Bundy, K. 2005, ApJ, 635, 1006
Shapley, A. E., Reddy, N. A., Kriek, M., et al. 2015, ApJ, 801, 88
Shimakawa, R., Kodama, T., Steidel, C. C., et al. 2015, MNRAS, 451, 1284
Shirazi, M., Brinchmann, J., & Rahmati, A. 2014, ApJ, 787, 120
Silverman, J. D., Kashino, D., Sanders, D., et al. 2015, ApJS, 220, 12
Silverman, J. D., Lamareille, F., Maier, C., et al. 2009, ApJ, 696, 396
Steidel, C. C., Rudie, G. C., Strom, A. L., et al. 2014, ApJ, 795, 165
Steidel, C. C., Strom, A. L., Pettini, M., et al. 2016, ApJ, 826, 159
Stott, J. P., Sobral, D., Bower, R., et al. 2013, MNRAS, 436, 1130
Tonegawa, M., Totani, T., Okada, H., et al. 2015, PASJ, 67, 81
Tremonti, C. A., Heckman, T. M., Kauffmann, G., et al. 2004, ApJ, 613 898
Valentino, F., Daddi, E., Strazzullo, V., et al. 2015, ApJ, 801, 132
van Zee, L., Salzer, J. J., Haynes, M. P., O'Donoghue, A. A., & Balonek, T. J. 1998, AJ, 116, 2805
Veilleux, S., & Osterbrock, D. E. 1987, ApJS, 63, 295
Whitaker, K. E., Franx, M., Leja, J., et al. 2014, ApJ, 795, 104
Wink, J. E., Wilson, T. L., & Bieging, J. H. 1983, A&A, 127, 211
Wuyts, E., Kurk, J., Förster Schreiber, N. M., et al. 2014, ApJL, 789, L40
Xue, Y. Q., Brandt, W. N., Luo, B., et al. 2010, ApJ, 720, 368
Yabe, K., Ohta, K., Akiyama, M., et al. 2015, PASJ, 67, 102
Yabe, K., Ohta, K., Iwamuro, F., et al. 2012, PASJ, 64, 60
Yabe, K., Ohta, K., Iwamuro, F., et al. 2014, MNRAS, 437, 3647
Yamada, T., Kajisawa, M., Akiyama, M., et al. 2009, ApJ, 699, 1354
Yates, R. M., Kauffmann, G., & Guo, Q. 2012, MNRAS, 422, 215
Zahid, H. J., Dima, G. I., Kudritzki, R.-P., et al. 2014a, ApJ, 791, 130
Zahid, H. J., Kashino, D., Silverman, J. D., et al. 2014b, ApJ, 792, 75
Zahid, H. J., Kewley, L. J., & Bresolin, F. 2011, ApJ, 730, 137